

1 **Residential burning is a potentially significant source of soluble iron to the**
2 **ocean**

3
4 Rui Li,^{1,#,a} Haley E. Plaas,^{2,#,b} Yifan Zhang,^{1,3} Yizhu Chen,^{1,3} Tianyu Zhang,^{1,3} Yi Yang,⁴ Sagar
5 Rathod,⁵ Guohua Zhang,¹ Xinming Wang,¹ Douglas S. Hamilton,^{2,*} Mingjin Tang^{1,6,*}

6
7 ¹ State Key Laboratory Advanced Environmental Technology and Guangdong Key Laboratory
8 of Environmental Protection and Resources Utilization, Guangzhou Institute of
9 Geochemistry, Chinese Academy of Sciences, Guangzhou, China

10 ² Marine, Earth, and Atmospheric Sciences, North Carolina State University, Raleigh, NC,
11 USA

12 ³ College of Earth and Planetary Sciences, University of Chinese Academy of Sciences, Beijing,
13 China

14 ⁴ Key Laboratory of Geographic Information Science of the Ministry of Education, School of
15 Geographic Sciences, East China Normal University, Shanghai, China

16 ⁵ Department of Atmospheric, Oceanic, and Space Sciences, University of Wisconsin-Madison,
17 Madison, WI, USA

18 ⁶ Institute of Surface-Earth System Science, School of Earth System Science, Tianjin
19 University, Tianjin, China

20
21 ^a Current affiliation: School of Public Health, MOE Key Laboratory of Coal Environmental
22 Pathogenicity and Prevention, Shanxi Medical University, Taiyuan, China

23 ^b Current affiliation: Columbia University, Center for Climate Systems Research, New York,
24 NY 10025, USA; NASA Goddard Institute for Space Studies, New York, NY, USA

25

26 **Correspondence:**

27 Mingjin Tang (mingjintang@126.com)

28 Douglas S. Hamilton (dshamil3@ncsu.edu)

29

30 # The two authors contributed equivalently to this work.

31

32

33 **Abstract**

34 Understanding the physicochemical processes that supply atmospheric aerosol iron (Fe) to the
35 ocean is crucial for understanding of global biogeochemical cycles. Anthropogenic activity
36 contributes significant fluxes of aerosol Fe to the atmosphere, the soluble fraction of which can
37 modulate marine primary productivity upon its deposition to the ocean surface. However,
38 anthropogenic aerosol Fe solubility remains poorly constrained, due in part to a lack of direct
39 measurements spanning a multitude of anthropogenic sources. We measured solubility of
40 aerosol Fe from several distinct anthropogenic combustion processes and fuel types. The
41 median Fe solubility varied widely by source, ranging from 0.03% for power plant coal fly ash
42 to 55.87% for biofuel burning; furthermore, residential coal burning aerosol possessed much
43 higher Fe solubility than power plant coal fly ash. Using the new Fe solubilities reported herein,
44 we updated parameters for anthropogenic aerosol Fe within the Community Earth System
45 Model. Anthropogenic combustion is estimated to contribute up to 20% of the global soluble
46 Fe flux to the ocean in the present day. Furthermore, we identified residential coal burning as
47 a previously neglected but potentially important source with regional flux contributions
48 ranging from <1% to 21%. Our work underscores the need to further refine understanding of
49 aerosol Fe properties from a wide variety of anthropogenic sources by increasing observations
50 in more novel aerosol regimes, with a focus on residential coal burning. This understanding
51 will in turn aid in characterizing the influences of anthropogenic activity on past, present, and
52 future atmospheric nutrient inputs to marine ecosystems.

53

54 **1 Introduction**

55 Anthropogenic activities have altered the atmospheric burden and deposition fluxes of
56 biogeochemically relevant trace metals, including iron (Fe) (Bergas-Massó et al., 2023;
57 Hamilton et al., 2020b). The quantity of Fe in ocean waters plays a particularly important role
58 in modulating the spatiotemporal distribution of primary productivity in ocean ecosystems,
59 which has downstream impacts on marine fisheries and carbon sequestration (Ito et al., 2021;
60 Tagliabue et al., 2014; Tagliabue et al., 2017). Energy-production, transportation, shipping,
61 and manufacturing (e.g., steel production) are all characterized sources of anthropogenic
62 aerosol Fe (Ito and Miyakawa, 2023; Ito and Shi, 2016; Rathod et al., 2024). These differing
63 combustion fuel types possess distinct physicochemical properties that influence their impact
64 on radiative forcing and nutrient supply (Al-Abadleh et al., 2023; Ito et al., 2018; Matsui et al.,
65 2018; Rathod et al., 2020).

66 To assess the potential nutritional impact of atmospheric Fe deposition on ocean
67 ecosystems, atmospheric aerosol research primarily focuses on tracing the soluble Fe content
68 in aerosol (Baker et al., 2020; Ito et al., 2019; Mahowald et al., 2018). Soluble Fe content is
69 often expressed as the fraction of soluble to total Fe in aerosol and then reported as a percentage
70 solubility (Baldo et al., 2022; Liu et al., 2022; Mahowald et al., 2009). Several key processes
71 control solubility of aerosol Fe over the course of its lifetime: 1) Fe mineralogy, 2) interactions
72 with acidic and organic species in aerosol and cloud water, and 3) particle size and surface area
73 to volume ratios (Bergas-Massó et al., 2023; Journet et al., 2008; Mcdaniel et al., 2019).
74 Anthropogenic combustion not only alters the magnitude and spatial distribution of Fe fluxes
75 from the atmosphere and to the surface ocean, but also influences the composition of the

76 atmosphere, that in turn, influences dissolution chemistry of aerosol Fe both directly and
77 indirectly. Mixing of aerosol Fe with acidic (e.g., sulfates or nitrates) and organic species (e.g.,
78 oxalate) co-emitted during anthropogenic combustion increases its solubility during transport
79 (Bergas-Massó et al., 2023; Chen et al., 2024; Itahashi et al., 2022; Li et al., 2017; Longo et al.,
80 2016). Furthermore, diverse technologies utilized during combustion processes (i.e., variable
81 combustion temperatures, boilers vs. furnaces, degree of emission control, and the fuel quality)
82 also influence the physicochemical properties of aerosol Fe beyond the composition of fuel
83 alone. As a result, studies examining socioeconomic, technology, and policy driven changes to
84 anthropogenic fuel-burning are needed to anticipate impacts on the global Fe cycle (Hamilton
85 et al., 2020b).

86 When compared to mineral dust, anthropogenic emissions of aerosol Fe are several orders
87 of magnitude lower at the global scale; however, anthropogenic Fe has a higher fractional
88 solubility (Ito et al., 2021), and the relative contribution of soluble Fe from anthropogenic
89 combustion is spatially distinct from dust (Hamilton et al., 2020b; Hamilton et al., 2019).
90 Therefore, anthropogenic activity can be a major contributor to Fe fluxes in many high nutrient
91 low chlorophyll (HNLC) ocean regions (Hawco et al., 2025; Liu et al., 2022).

92 Despite the importance of understanding anthropogenic Fe fluxes, the fractional solubility
93 of aerosol Fe emitted from various anthropogenic sources remains poorly understood
94 (Desboeufs et al., 2005; Li et al., 2022b; Oakes et al., 2012); consequently, Fe solubility
95 parameterizations in modeling studies for anthropogenic Fe vary widely (Ito et al., 2019;
96 Myriokefalitakis et al., 2018). In this work, we measured the Fe content and solubility for
97 aerosol emitted by several important anthropogenic sources (i.e., coal power plants, steelwork

98 industry, municipal water combustion, oil combustion, residential coal, and biofuel burning).
99 Then, using an Earth System Model, we applied the experimental results by updating Fe
100 solubility parameters for distinct anthropogenic combustion fuel-sources. Simulated Fe
101 concentrations and solubilities were validated against a global observational Fe aerosol dataset
102 at the regional scale. Then, the model was used to quantify and bound uncertainties in emission
103 and deposition fluxes of soluble Fe under three anthropogenic combustion emission scenarios
104 spanning past (pre-industrial) to future (Shared Socioeconomic Pathway 3-7.0, SSP370)
105 conditions.

106 **2 Methodology**

107 The experimental and modelling methods employed in this work are described in Sections
108 2.1 and 2.2, respectively.

109 **2.1 Experimental methods**

110 This work examined six types of anthropogenic combustion aerosol, which were classified
111 into two broad categories. The first category, fly ash, included power plant coal fly ash,
112 steelwork fly ash, municipal waste fly ash, and oil fly ash. The second category, residential fuel
113 sources, included residential coal and biofuel combustion. Biofuels examined in this work were
114 limited to straw, wood, grasses and leaves, and we did not examine other biofuels such as dung.

115 **2.1.1 Fly ash and bottom ash samples**

116 The volume-mean diameters, determined using diameter light scattering, were found to
117 be 16.9-67.6, 4.7-176.4, 21.2-115.9 and 15.4 μm for power plant coal fly ash (n=31), steelwork
118 fly ash (n=29), municipal waste fly ash (n=3), and oil fly ash (n=1) samples, respectively (Li,
119 2025).

120 Power plant coal fly ash samples were obtained from electrostatic precipitators or
121 baghouse rows in coal power plants in 29 provinces in China (Li et al., 2021; Liu et al., 2021);
122 one coal power plant was selected in each province except for Guangdong and Shandong where
123 two coal power plants were selected for each province. As a result, 31 power plant coal fly ash
124 samples were examined in total. In addition, we examined 29 steelwork fly ash samples
125 collected from different iron and steel plants, three municipal waste fly ash samples (Li et al.,
126 2022b; Li et al., 2021), and two oil fly ash samples which were PM_{2.5} samples emitted by heavy
127 oil and diesel fuel combustion in the engine of a cargo ship (Wu et al., 2018), and one oil
128 bottom ash sample (Fu et al., 2012). As the numbers of municipal waste and oil ash samples
129 were limited, we include their results data in the supplement, but do not discuss them further
130 in the main paper due to a lack of statistical significance.

131 Fly ash and bottom ash samples (~10 mg for each sample) were digested and then
132 analyzed using inductively coupled plasma mass spectrometry (ICP-MS) to determine their Fe
133 content. Experimental procedures for sample digestion and total Fe measurement can be found
134 elsewhere (Li et al., 2022c). Soluble Fe was leached and determined using the procedure
135 described in our previous work (Li et al., 2022b). In brief, fly ash and bottom ash samples (~20
136 mg for each sample) were individually leached in 20 mL sodium acetate buffer (5 mmol/L, pH
137 = 4.3) for 2 h, during which an orbital shaker (300 rpm) was used to stir the solution. The
138 aqueous mixture was centrifuged (3000 rpm) for 15 min, and a pH paper (range: 3.5-6.8;
139 precision: 0.3; Macherey-Nagel, Germany) was used to measure the pH of the solution and no
140 measurable pH change occurred after leaching. The aqueous solution was filtered through a
141 polyethersulfone filter (pore size: 0.22 μm), acidified to contain 1% (v/v) nitric acid and then

142 analyzed by ICP-MS to measure soluble Fe. In this work, fractional solubility of Fe was
143 reported as the ratio (in %) of soluble Fe to total Fe.

144 A wide range of protocols, differing in leaching solution, filter pore size, and so on, were
145 used to extract soluble Fe, and the results obtained using different leaching protocols could be
146 substantial (Tang et al., 2025). Sodium acetate buffer, instead of ultrapure water, was used in
147 the present work as the leaching solution, because its pH did not change during leaching due
148 to its larger buffering capacity compared to ultrapure water.

149 **2.1.2 Residential coal and biofuel combustion aerosols**

150 Generation and collection of residential coal and biofuel combustion aerosols are detailed
151 in the Supplement (Text S1). In brief, we burned coal and biofuel in a commercial cook stove
152 widely used in rural areas in China and collected PM_{2.5} samples (aerosol particles with
153 aerodynamic particle diameters below 2.5 μm) onto pre-cleaned Whatman 41 (W41) cellulose
154 filters using a medium volume aerosol sampler (TH-150C, Tianhong Co.).

155 Our work examined three types of coal (anthracite, semibituminous coal, and bituminous
156 coal) and nine types of biofuel (wheat straw, rice straw, corn straw, rape straw, cogongrass,
157 China fir trunk, pine trunk, poplar trunk, and pine needle) commonly found in China. We
158 collected eight filter samples for each fuel type, except anthracite for which we only collected
159 two filter samples. We had to combine some filter samples in our experimental analysis to meet
160 the detection limit for soluble Fe; as a result, the number of effective filter samples (for which
161 Fe content and solubility were reported) were usually <8 for each fuel type (see Tables S2 and
162 S4 for further information).

163 After aerosol collection, the filters were individually placed in a pre-cleaned Petri dish
164 and then stored in a desiccator for 60 h to remove particle-associated water. The mass of filters
165 before and after aerosol collection were measured (accuracy of 0.1 mg), and the mass of
166 particles collected ranged from 2.5 to 432.7 mg. Each filter was then divided into two equal
167 parts. To determine the soluble Fe content, the first half of a filter was leached in 20 mL sodium
168 acetate buffer (5 mmol/L, pH = 4.3) for 2 h (Section 2.1.1) and analyzed using ICP-MS. Fe
169 concentrations in some leaching solutions were low; as a result, these leaching solutions (~15
170 mL for each solution) were combined for the same fuel type and then pre-concentrated to a
171 volume of 6 mL, in order to increase Fe concentration in the solution used for ICP-MS analysis.
172 The second half of a filter was digested and analyzed by ICP-MS to determine total Fe, and the
173 experimental procedure used can be found in our previous work (Zhang et al., 2022). If leaching
174 solutions were combined for the first parts of these filters, their second parts were also
175 combined and digested together to allow direct comparison.

176 **2.1.3 Quality assurance and quality control**

177 The detection limit of Fe in solution was determined to be 0.5 $\mu\text{g/L}$ in this work. A
178 reference solution (NIST 1643f) was used to check the accuracy of ICP-MS analysis, and the
179 difference between actual and measured concentrations was found to be <1%. Furthermore,
180 three blanks (with no fly ash or filters not loaded with any particles) were used in each batch
181 when we measured total or soluble Fe. The background levels of soluble Fe were always below
182 the detection limit; the background levels of total Fe, ranging from 4.3-5.7 $\mu\text{g/L}$, were much
183 lower than total Fe concentrations for most of our samples and subtracted when we reported
184 our results.

185 **2.2 Model simulations**

186 **2.2.1. Atmospheric Fe model description**

187 Earth System Models can investigate the spatiotemporal distribution and fluxes of key
188 atmospheric nutrients under various climatological regimes (Hamilton et al., 2020b; Hamilton
189 et al., 2022; Wu et al., 2020). To test the impact of new soluble Fe parameters (Section 2.1) on
190 modeled fluxes of soluble aerosol Fe to the atmosphere and marine ecosystems, we used the
191 Mechanism of Intermediate complexity for Modeling Iron (MIMI). MIMI is an Fe aerosol-
192 chemistry module embedded within the atmospheric component (Community Atmosphere
193 Model version 6, CAM6) of the Community Earth System Model version 2 (CESM2)
194 (Danabasoglu et al., 2020; Hamilton et al., 2019). Mineral dust, anthropogenic combustion,
195 and wildfire emissions are currently represented as distinct sources of aerosol Fe in MIMI. The
196 current dust emission scheme within MIMI includes an updated soil moisture submodule
197 within the land component of the model that prognostically calculates dust aerosolization as a
198 function of soil moisture (Li et al., 2022a). Following the implementation of a new soil-
199 moisture scheme, dust was rescaled to attain a global climatological mean dust aerosol optical
200 depth of ~ 0.03 (Ridley et al., 2016), consistent with all previous versions of the MIMI model.
201 The inclusion of these improvements to dust and updated anthropogenic Fe sources represents
202 a new working version of MIMI v1.1, as described herein, and detailed validation efforts are
203 reported in the Supplement (Figure S3 and Table S11).

204 A comprehensive overview of model details and parameters is provided in Hamilton et al.
205 (2019); in brief, MIMI simulates the emission, atmospheric transport, and deposition of Fe-
206 containing aerosol within three distinct particle size modes (Aitken, accumulation, and coarse

207 modes). Within each source of aerosol Fe (dust, wildfire, and anthropogenic combustion), both
208 the insoluble and soluble fractions are carried as separate tracers, and the soluble fraction of Fe
209 for each aerosol source is assigned at the point of emission. Prior to deposition and during
210 atmospheric transport, Fe solubility is further modified via non-reversible multiphase reactions
211 with acidic and organic species. Acidic processing is a function of aerosol pH and temperature
212 (Meskhidze et al., 2005), while organic processing is an aqueous phase chemistry reaction that
213 depends on oxalate concentrations which are calculated based on the concentrations of
214 secondary organic aerosol present (Johnson and Meskhidze, 2013; Scanza et al., 2018).

215 The model is gridded in a 3-dimensional space at a resolution of 0.96×1.25 degrees
216 (latitude \times longitude) and includes 56 vertical pressure levels from the surface to 2 hPa at the
217 highest altitude. Meteorology is forced in all the simulations using Modern-Era Retrospective
218 analysis for Research and Applications Version 2 (MERRA-2), and a 1-year model spin up
219 was undertaken for all simulations.

220 **2.2.2 Global pyrogenic Fe emission inventories and input dataset development**

221 While dust Fe emissions are calculated prognostically within MIMI, anthropogenic and
222 wildfire (sum of these being pyrogenic) emissions are prescribed using emissions inventories.
223 Annual mean anthropogenic Fe emission fluxes were inputted to the model using a modified
224 version of an inventory first developed in Rathod et al. (2020) and further detailed in Rathod
225 et al. (2024). In this inventory, Fe content in combustion aerosol was empirically derived for
226 the present day (PD; climatological year 2010) using the Speciated Pollution Emissions Wizard
227 (SPEW) (Bond et al., 2007; Bond et al., 2004), which characterizes anthropogenic emissions
228 of particulate matter by fuel-source and combustion technology. Soluble and insoluble Fe

229 content are dependent on fuel-type and also segregated by key sectors: 1) industrial fossil fuel
 230 (coal), 2) industrial and vehicular fossil fuels (oil), 3) smelting operations (steel/iron), and 4)
 231 residential cooking/heating (biofuel/biomass/wood) (Rathod et al., 2020). Industrial oil
 232 emissions were separated by land- and sea-based emissions to distinguish terrestrial
 233 transportation from shipping. Wildfire-Fe emission parameters are detailed in Hamilton et al.
 234 (2019), and in this work we used the CMIP6 (Coupled Model Intercomparison Project phase
 235 six) fire emission inventory for PD simulations (Van Marle et al., 2017).

236 Here, for the first time, we separated anthropogenic coal Fe into distinct industrial and
 237 residential sources and tested two approaches to constrain the magnitude of the residential Fe
 238 signal, i.e. a high emission scenario and a low emission scenario. To create the first inventory
 239 ('high-residential' emissions), we multiplied a series of spatially-resolved ($1^\circ \times 1^\circ$ grid box)
 240 ratios of residential-to-industrial black carbon (BC) emissions to the Rathod et al. (2024) Fe
 241 inventory emissions for coal. The BC ratios (Eqs. 1a and 1b) were derived from the CMIP6 BC
 242 emission dataset (Hoesly et al., 2018):

$$243 \quad [Fe_{RESI}]_{i,j,HIGH} = \frac{[BC_{RESI}]_{i,j,H}}{[BC_{IND}]_{i,j,H}} \times [Fe_{IND+RESI}]_{i,j,R} \quad (1a)$$

$$244 \quad [Fe_{IND}]_{i,j,HIGH} = \frac{[BC_{IND}]_{i,j,H}}{[BC_{RESI}]_{i,j,H}} \times [Fe_{IND+RESI}]_{i,j,R} \quad (1b)$$

245 Where i and j represent the longitudinal and latitudinal coordinates, $RESI$ and IND represent
 246 residential and industrial sources, $HIGH$ represents the high-residential inventory being
 247 constructed, H represents the Hoesly et al. (2018) dataset, R represents the Rathod et al. (2024)
 248 dataset, and $[Fe]$ and $[BC]$ represent their respective speciated fluxes in units of $\text{kg m}^{-2} \text{s}^{-1}$.
 249 This approach was chosen to capture spatial variations in coal burning technologies within the

250 inventory but assumed that residential Fe-to-industrial Fe emissions track residential BC-to-
251 industrial BC.

252 To create the second inventory ('low-residential' emissions) we globally scaled the high-
253 residential inventory to reflect potential differences in fuel-type specific emissions. To do so,
254 we used fuel-type specific Fe emissions reported in Rathod et al. (2020) and fuel-type specific
255 BC emissions reported in Bond et al. (2004). The CMIP6 anthropogenic emissions dataset of
256 Hoesly et al. (2018) classifies emission sectors as: 0) agriculture, 1) energy, 2) industrial, 3)
257 terrestrial transportation, 4) residential/commercial/other, 5) solvents production/application,
258 6) waste, and 7) international shipping. Therefore, emissions labeled either commercial or
259 residential in Rathod et al. (2020) were grouped into 'residential' to pair them with CMIP6.
260 We also treated 'energy' and 'industrial' sources together as industrial coal BC and ocean-
261 masked 'international shipping' with land-masked 'terrestrial transportation' together as oil BC
262 sources. Hoesly et al. (2018) does not separate residential biofuel (wood) from residential coal,
263 and these two sources are under separate investigation within this study; as a result, we used
264 the ratio of residential coal to all residential sources reported in Bond et al. (2004) to separate
265 the Hoesly residential BC emissions (Table S8), assuming parity between BC datasets. Then,
266 we calculated the ratio of residential Fe-to-residential BC and industrial Fe-to-industrial BC
267 (Eq. 2a; Table S8), resulting in a scaling factor of 0.035. This scaling factor was then applied
268 to the high-residential emissions to create the low-residential Fe emissions inventory (Eqs. 2b
269 and 2c):

$$270 \quad \frac{[Fe_{RESI}]_{R^*} / [BC_{RESI}]_{H^*}}{[Fe_{IND}]_{R^*} / [BC_{IND}]_H} = 0.035 \quad (2a)$$

$$271 \quad [Fe_{RESI}]_{i,j,LOW} = [Fe_{RESI}]_{i,j,HIGH} * 0.035 \quad (2b)$$

$$[Fe_{IND}]_{i,j,LOW} = [Fe_{IND}]_{i,j,HIGH} * (1 - 0.035) \quad (2c)$$

where H^* denotes data from Hoesly et al. (2018) scaled by the Bond et al. (2004) BC inventory to isolate residential coal, R^* denotes data from Rathod et al. (2020), and LOW denotes the low-residential inventory. By redistributing residential and industrial coal Fe emissions using these sector-specific ratios of Fe-to-BC to create the low-residential emissions inventory, residential coal emissions were reduced by one order of magnitude at the global scale when compared to the high-residential emissions inventory (16 Gg a⁻¹ vs 460 Gg a⁻¹; Table S9). Both inventories were applied and tested with each PD model simulation to perform a sensitivity analysis that quantified the uncertainty in residential coal Fe emissions introduced by each new inventory.

Once sector-specific emissions inventories were read into the model, fuel-sources were summed to total one anthropogenic tracer. This tracer is then separated into soluble and insoluble fractions with three modes within the model code (Eqs. 3a and 3b). This results in six anthropogenic combustion-Fe tracers in total to be transported within the model, as follows:

$$[Fe_{insol}]_a = \Sigma\{[Fe_X]_{i,j,a,b} * (1 - sol_b)\} \quad (3a)$$

$$[Fe_{sol}]_a = \Sigma ([Fe_X]_{i,j,a,b} * sol_b) \quad (3b)$$

where X denotes the emissions scenario, a represents the aerosol mode (fine or coarse), b represents the fuel-source (industrial oil, industrial coal, residential coal, residential biofuel, or smelting), $insol$ represents the insoluble fraction, sol represents the soluble fraction, and sol_b represents the fractional solubility for each fuel-source (b). As a final step, the fine mode was split into accumulation and Aitken modes by applying a ratio of 9:1.

293 2.2.3 Model simulations performed

294 Thirteen model simulations were performed to evaluate the impact of anthropogenic
 295 combustion aerosol solubility updates (Section 2.1) on atmospheric soluble Fe fluxes to key
 296 marine ecosystems (Table 1). For all simulations, we set the model climatology to present-day
 297 (PD) conditions, spanning 2009-2011 inclusive. Simulations were distinguished as cases
 298 (variable Fe solubility parameterizations) within different emission scenarios (variable
 299 anthropogenic combustion emission fluxes).

300

301 **Table 1.** Description of model simulations performed using MIMI with emission scenarios and
 302 emission inventories either directly inputted (Fe) to the model or utilized to generate the Fe
 303 inventory (BC). PD = present day (2010 CE), PI = pre-industrial (1750 CE), SSP370 = Shared
 304 Socioeconomic Pathway scenario 3-7.0, MID = midcentury (2040-2050 CE) and END = end
 305 century (2090-2100 CE). NA = assumed industrial activity is zero at 1750 CE.

| Emissions Scenario | Simulation | Fe Emissions Inventory | BC Emissions database | BC Emission (Tg a ⁻¹) |
|--------------------|-----------------|------------------------|-----------------------------------------|-----------------------------------|
| PD | PD-BASE | Rathod et al., 2024 | Hoesly et al., 2018 | 6.46 |
| PD | PD-RESI | High-Residential | Hoesly et al., 2018 | 6.46 |
| PD | PD-BIOF | High-Residential | Hoesly et al., 2018 | 6.46 |
| PD | PD-IND | High-Residential | Hoesly et al., 2018 | 6.46 |
| PD | PD-BASE | Rathod et al., 2024 | Bond et al., 2004 & Hoesly et al., 2018 | 6.46 |
| PD | PD-RESI | Low-Residential | Bond et al., 2004 & Hoesly et al., 2018 | 6.46 |
| PD | PD-BIOF | Low-Residential | Bond et al., 2004 & Hoesly et al., 2018 | 6.46 |
| PI | PI-BASE | Hamilton et al., 2020a | NA | NA |
| PI | PI-BIOF | Hamilton et al., 2020a | NA | NA |
| FU (2050) | MID-SSP370-BASE | High-Residential | SSP3.70 | 8.30 |
| FU (2050) | MID-SSP370-BIOF | High-Residential | SSP3.70 | 8.30 |
| FU (2100) | END-SSP370-BASE | High-Residential | SSP3.70 | 6.33 |
| FU (2100) | END-SSP370-BIOF | High-Residential | SSP3.70 | 6.33 |

306

307 The first seven simulations (i.e., PD simulations) aimed to assess the impact of each new
308 solubility parameter on the ability of the model to capture ship-based observations of total Fe,
309 soluble Fe, and Fe solubility. These simulations applied the high-residential emissions
310 inventory (Section 2.2.2), and were repeated using the low-residential Fe inventory with the
311 exception of PD-IND (Table 1). The first PD case in each set (i.e., PD-BASE) served as a
312 baseline, i.e., no changes were made to solubility when compared to previous studies using
313 MIMI. Residential coal was distinguished from industrial coal emissions, but this had no
314 impact on soluble Fe fluxes since the same fractional solubility (0.2%) was applied to both
315 sources (Rathod et al., 2020; Rathod et al., 2024). In the next three PD cases (PD-RESI, PD-
316 BIOF, PD-IND), fractional solubility was updated incrementally for individual sectors to
317 assess fuel-type specific impacts to soluble Fe fluxes, which are later detailed in Section 3.3;
318 results from PD-IND are reported in the Supplement. Information on model validation and
319 constraint to ship-based observations of aerosol Fe is provided in Section 2.2.5.

320 Using both pre-industrial (PI; 1750 CE) and future (FU; 2050 and 2100 CE) anthropogenic
321 emissions scenarios, we performed six model simulations to examine the impacts of changes
322 in anthropogenic activity on Fe fluxes over time. In each pair of simulations, we applied
323 the -BASE solubility parameters to establish a baseline and the -BIOF solubility parameters to
324 examine an upper bound for residential soluble Fe fluxes. Accordingly, we also used the high-
325 residential Fe emissions inventory framework in development of the FU emissions inventory
326 to further establish a maximum estimate for anthropogenic soluble Fe through the end of the
327 21st century. To isolate how changes in soluble aerosol Fe fluxes responded to changes in

328 emission parameterizations and subsequent dissolution chemistry in the model, PI and FU
329 simulations were conducted with meteorological and climatological conditions identical to the
330 PD (2009-2011).

331 The PI simulations (PI-BASE and PI-BIOF) served as a reference point for comparison to
332 PD and FU simulations, per minimal influence on the Fe cycle by anthropogenic emissions
333 (Table 1). MID-SSP370-BASE, MID-SSP370-BIOF, END-SSP370-BASE, and END-
334 SSP370-BIOF were conducted to evaluate the projected impact of population increases and
335 socioeconomic changes to energy production and fuel-usage over the course of the century.
336 We selected the highest air pollution emissions scenario of the Shared Socio-economic
337 Pathways (SSPs) as detailed in SSP 3-7.0 (SSP370), the “regional rivalry” scenario, which
338 represents anticipated sociopolitical and environmental changes resulting in an increase to
339 radiative forcing by 3-7.0 W m⁻² by the year of 2100 (Riahi et al., 2017). Given that BC
340 emissions are anticipated to peak in the midcentury (2040-2050) but return to PD-comparable
341 emissions by 2100 (Turnock et al., 2020), we assessed projected changes to Fe emissions at
342 both the mid-point (2050) and endpoint of the 21st century (2100). Dust fluxes in future Fe
343 emission scenarios were adjusted to account for dust-climate feedback using a scaling factor
344 ranging between 1.0-1.1, as described in Hamilton et al. (2020a).

345 **2.2.4 Preindustrial (PI) and future (FU) Fe emission estimates**

346 For PI simulations, we used a pre-developed Fe combustion emission inventory (Hamilton
347 et al., 2020b). Only residential (wood) biofuel burning served as an anthropogenic source of
348 Fe due to a presumable lack of industrialized anthropogenic emissions (i.e., fossil fuels and
349 smelting; (Hamilton et al., 2020a); global emission for anthropogenic combustion was 0.7×10^7

350 $^3 \text{ Gg Fe a}^{-1}$ and only occupied the fine aerosol mode (i.e., sum of Aitken and accumulation
351 modes). Details on the development of the PI Fe combustion emission inventory are provided
352 in Hamilton et al. (2020b).

353 For FU simulations, we developed two new Fe emissions datasets (for 2050 and 2100)
354 which were both derived from our high-residential emissions inventory developed for the PD
355 simulations. Fe emissions were linearly scaled for all combustion sources according to
356 projected changes in anthropogenic BC emissions via the decadal CMIP6 anthropogenic BC
357 emission dataset for 2040-2050 and 2090-2100 (Hoesly et al., 2018; Riahi et al., 2017). BC
358 emissions labeled ‘residential, commercial and other’ were separated into residential coal and
359 residential biofuel sources of BC based on the grid-cell specific ratios of residential coal Fe to
360 residential biofuel Fe in our high-residential emissions inventory.

361 Following a similar approach to the PD high-residential emissions inventory, using a grid-
362 cell resolved dynamic ratio of Fe-to-BC, that was grouped based on sector and aerosol size
363 fraction, we calculated FU Fe emissions tracking CMIP6 projected BC emissions (Eq. 4), as
364 follows:

$$365 \quad \frac{[Fe_X]_{i,j,a,b}}{[BC_X]_{i,j,a,b}} = \frac{[Fe_{PD}]_{i,j,a,b}}{[BC_{PD}]_{i,j,a,b}} \quad (4)$$

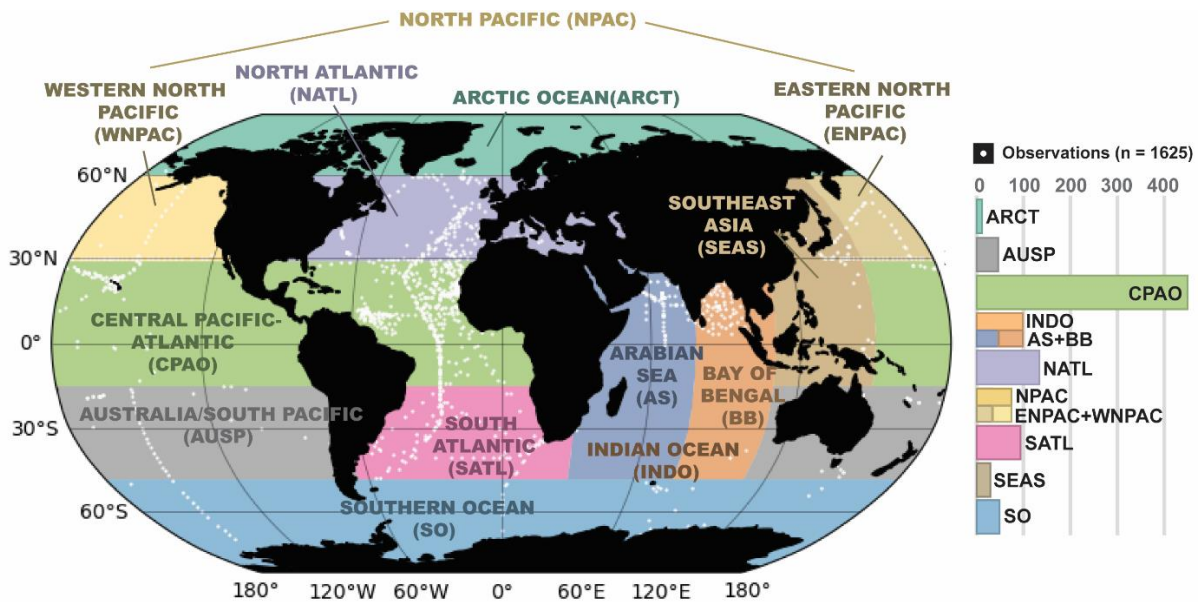
366 where X denotes the emissions scenario (MID-SSP370 or END-SSP370), i and j represent the
367 longitudinal and latitudinal coordinates, a represents the aerosol mode (fine or coarse), b
368 represents the fuel-source (industrial oil, industrial coal, residential coal, residential biofuel, or
369 smelting), and [Fe] and [BC] represent the speciated fluxes ($\text{kg m}^{-2} \text{ s}^{-1}$). BC emissions from
370 smelting operations were not directly available for PI or FU projections; therefore, they were
371 set to 0.0 in the PI and maintained at PD levels in the FU. By using SSP370, the -BIOF case

372 solubility parameters, and the high-residential emissions inventory, our FU simulations
373 established an upper bound estimate for future anthropogenic soluble Fe fluxes as based on
374 current observational uncertainties. The SimFire inventory, coupled to the LPJ-GUESS (Lund-
375 Potsdam-Jena General Ecosystem Simulator) vegetation model, was used to prescribe wildfire-
376 Fe emissions during the PI era (Hamilton et al., 2018; Hamilton et al., 2020a; Knorr et al., 2016)
377 For wildfire-Fe emissions in FU scenarios, we used the CMIP6 fire emission datasets for MID-
378 SSP370 and END-SSP370 (Bergas-Masso et al., 2025; Hamilton et al., 2024).

379 **2.2.5 Model validation**

380 To evaluate model performance, we compared global observations of total Fe
381 concentration, soluble Fe concentration, and Fe solubility to modeled values for each PD
382 simulation, grouping data by key aerosol deposition and ocean biogeochemistry regions. The
383 observational dataset of Fe content in aerosol was reported in Hamilton et al. (2019) and
384 updated herein to include measurements from Srinivas et al. (2012) and more recent studies
385 published between 2021 and 2024 (n = 1624) (Desboeufs et al., 2024; Elliott et al., 2024;
386 Kurisu et al., 2021; López-García et al., 2021; Marafante et al., 2024; Panda et al., 2022; Perron
387 et al., 2022; Rodríguez et al., 2021; Sakata et al., 2022; Seo and Kim, 2023; Winton et al., 2022;
388 Wu et al., 2023; Zhang et al., 2024). Observed Fe solubility in aerosol spans five orders of
389 magnitude (Perron et al., 2024), and one reason for this large range is due to differences in
390 experimental procedures during quantification (Tang et al., 2025). To facilitate a more direct
391 comparison between modeled and observed soluble Fe content, we removed observations from
392 the global dataset that did not measure soluble Fe directly. When multiple observations fell
393 within a model grid cell, values were aggregated to climatological averages, using medians to

394 be most representative of expected variations in Fe fluxes across time and space (final n = 990;
 395 Figure 3). For final evaluation of the model capability in simulating surface Fe concentrations,
 396 both model and observational data were grouped into key ocean regions (Figure 1), based on
 397 predominant sources of atmospheric aerosol and phytoplankton nutrient limitation dynamics
 398 (i.e., HNLC regions) as revealed in Hamilton et al. (2019) and Hamilton et al. (2023). To
 399 quantitatively evaluate model skill, root mean square errors (RMSE) were calculated for the
 400 high-residential inventory cases and are provided in the Supplement.



401
 402 **Figure 1.** Regional groupings for model-observation comparisons of surface Fe concentrations
 403 (ship-based, in aerosol). The coordinates for individual Fe observations are indicated with a
 404 white circle. Number of soluble Fe observations within each region are provided by the
 405 histogram (n=990).

406

407 3 Results and Discussion

408 Sections 3.1 and 3.2 present Fe content and solubility measured in our experimental work.

409 The numbers of samples examined in our work are very small for municipal waste fly ash and

410 oil fly/bottom ash, and the results may not be representative; therefore, these results are mainly
 411 presented in the Supplement. Modeling results are presented in Section 3.3.

412 **3.1 Fe content by fuel type**

413 This work quantified the Fe content in particles from six different combustion and
 414 anthropogenic sources, including power plant coal fly ash, residential coal combustion aerosol,
 415 steelwork fly ash, residential biofuel burning aerosol, municipal waste fly ash, and oil fly ash
 416 (Table 2; Fe content in individual samples is provided in Tables S1-S5).

417
 418 **Table 2.** Summary of Fe content and solubility for power plant coal fly ash, residential coal
 419 combustion aerosol, steelwork fly ash, and biofuel burning aerosol examined in our work (*n*:
 420 number of samples examined in our work). Fe content and solubility for other samples
 421 examined in this work (i.e. municipal waste fly ash, oil fly ash and oil bottom ash) can be found
 422 in the Supplement.

| sample type | <i>n</i> | range | average | median |
|----------------------------------------|----------|-------------|-------------|--------|
| Fe content (mg/g) | | | | |
| power plant coal fly ash | 31 | 20.7-103.8 | 37.2±16.8 | 35.0 |
| residential coal combustion aerosol | 10 | 0.025-0.101 | 0.044±0.023 | 0.038 |
| steelwork fly ash | 29 | 5.8-918.9 | 312.6±246.1 | 346.5 |
| biofuel burning aerosol | 27 | 0.002-0.101 | 0.023±0.026 | 0.013 |
| Fe solubility (%) | | | | |
| power plant coal fly ash | 31 | 0.002-0.17 | 0.05±0.05 | 0.03 |
| residential coal combustion aerosol | 10 | 7.03-100 | 33.30±27.71 | 28.45 |
| steelwork fly ash | 29 | 0.007-10.64 | 1.37±2.77 | 0.07 |

423

424

425 **3.1.1 Power plant coal fly ash**

426 Fe content ranged from 20.7 to 103.8 mg/g for the 31 power plant coal fly ash samples
427 examined in our work, with average and median values being 37.2 ± 16.8 and 35.0 mg/g,
428 respectively. As shown in Table S6, Fe content ranged from 16.0 to 52.0 mg/g ($n = 3$) in one
429 study (Baldo et al., 2022), with mean and median values being 33.0 ± 18.0 and 31.0 mg/g; in
430 another study (Goodarzi, 2006), the median value of Fe content was determined to be 34.4
431 mg/g ($n = 7$). Fe content measured by these two studies (Baldo et al., 2022; Goodarzi, 2006)
432 agreed well with our work. Some other studies (Dutta et al., 2009; Fu et al., 2012; Jankowski
433 et al., 2006; Meij, 1994) found higher mean or median Fe content for power plant coal fly ash
434 (Table S6), but the reported ranges overlapped with our work. For example, Fe content were
435 found to range from 38.3 to 98.6 mg/g ($n = 7$) in one study (Li et al., 2022b), with mean and
436 median values being 62.1 ± 26.7 and 43.2 mg/g; in another study (Moreno et al., 2005), Fe
437 content were found to range from 18.2 to 112.0 mg/g ($n = 23$), with mean and median values
438 being 57.8 ± 22.7 and 52.5 mg/g.

439 In summary, the mean or median Fe content reported in different studies are typically in
440 the range of 30-70 mg/g for power plant coal fly ash, and this variability is likely due to
441 difference in coal (Wang et al., 2015; Ward, 2016) and combustion conditions (Blissett and
442 Rowson, 2012; Kutchko and Kim, 2006). Fe content in power plant coal fly ash was set to ~70

443 mg/g in some modeling studies (Luo et al., 2008; Rathod et al., 2020), being consistent with
444 experimental results.

445 **3.1.2 Residential coal combustion aerosol**

446 For the 10 residential coal combustion aerosol samples (PM_{2.5}) we examined, Fe content
447 ranged from 0.025 to 0.101 mg/g (Table 2), with average and median values being 0.044 ±
448 0.023 and 0.038 mg/g, respectively. Only a few previous studies measured Fe content in
449 residential coal combustion aerosols (Table S6). The average Fe content was determined by
450 Patil et al. (2013) to be 0.048 ± 0.035 mg/g (n = 3) for PM_{2.5} and 0.061 ± 0.044 mg/g (n = 3)
451 for PM₁₀, being similar to or slightly higher than our result. In another two studies (Watson et
452 al., 2001; Zhang et al., 2012), the average Fe content was measured to be 0.671 ± 0.023 mg/g
453 (n = 4) and 0.7 ± 0.1 mg/g (n = 5), significantly higher than our result, and such differences
454 may be attributed to variations in coal types and combustion conditions. Overall, our and
455 previous studies suggest that the Fe content in residential coal combustion aerosols is very low,
456 typically below 1 mg/g. Fe content were set to 1 and 0.5 mg in previous modeling studies (Luo
457 et al., 2008; Rathod et al., 2020), being broadly consistent with experimental results.

458 Fe content in power plant coal fly ash is much higher than residential coal combustion
459 aerosols, primarily due to differences in combustion conditions (Rathod et al., 2020). Power
460 plant coal fly ash has very low carbon content and is mainly composed of metals and minerals
461 (Ahmaruzzaman, 2010; Li et al., 2022c; Patil et al., 2013); in contrast, residential coal
462 combustion aerosol particles contain a large fraction of carbonaceous materials due to
463 incomplete combustion, and thus the content of metals, including Fe, are much lower (Patil et
464 al., 2013; Zhang et al., 2012). Furthermore, combustion temperature typically ranges from 1200

465 to 1700 °C for coal-fired power plant, enabling Fe in coal to enter fly ash particles through
466 volatilization-condensation (Blissett and Rowson, 2012); residential coal combustion occurs at
467 much lower temperatures which are insufficient for Fe to enter aerosols through this process
468 (Rathod et al., 2020), also leading to lower Fe content.

469 **3.1.3 Steelwork fly ash**

470 For the 29 steelwork fly ash samples we examined, Fe content ranged from 5.8 to 918.9
471 mg/g, with mean and median values measured to be 312.6 ± 246.1 and 346.5 mg/g, respectively
472 (Table 2). As shown in Table S6, some previous studies have reported average Fe content to
473 be 358.9 (n = 1), 369.3 (n = 1), 312.2 (n = 1), and 329.1 ± 22.6 mg/g (n = 4) (Alizadeh and
474 Momeni, 2016; Silva et al., 2019; Souza et al., 2010; Vieira et al., 2013), in good agreement
475 with our results. Lower Fe content was also reported by previous work, with average values
476 being 86.0 (n = 1), 128.1 (n = 1), 150.8 (n = 1), 286.5 (n = 1), 284.6 (n = 1), 238.7 (n = 1), and
477 267.3 ± 4.8 mg/g (n = 4) (Al-Negheimish et al., 2021; Alsheyab and Khedaywi, 2016; Laforest
478 and Duchesne, 2006; Li et al., 2023; Loaiza et al., 2017; Stathopoulos et al., 2013; Xia and
479 Picklesi, 2000); in contrast, some previous studies also found the average or mean Fe content
480 to be around 400-500 mg/g (Machado et al., 2006; Patil et al., 2013; Ye et al., 2021), slightly
481 higher than our results.

482 Despite some variability in Fe content reported by our and previous studies (Table S6),
483 the mean or median Fe content are generally around 300–500 mg/g for steelwork fly ash. In a
484 recent modeling study (Rathod et al., 2020), the Fe content in steelwork fly ash was set to 440
485 mg/g (and the lower and upper bounds were set to 150 and 950 mg/g), being consistent with
486 experimental results.

487 **3.1.4 Biofuel burning aerosol**

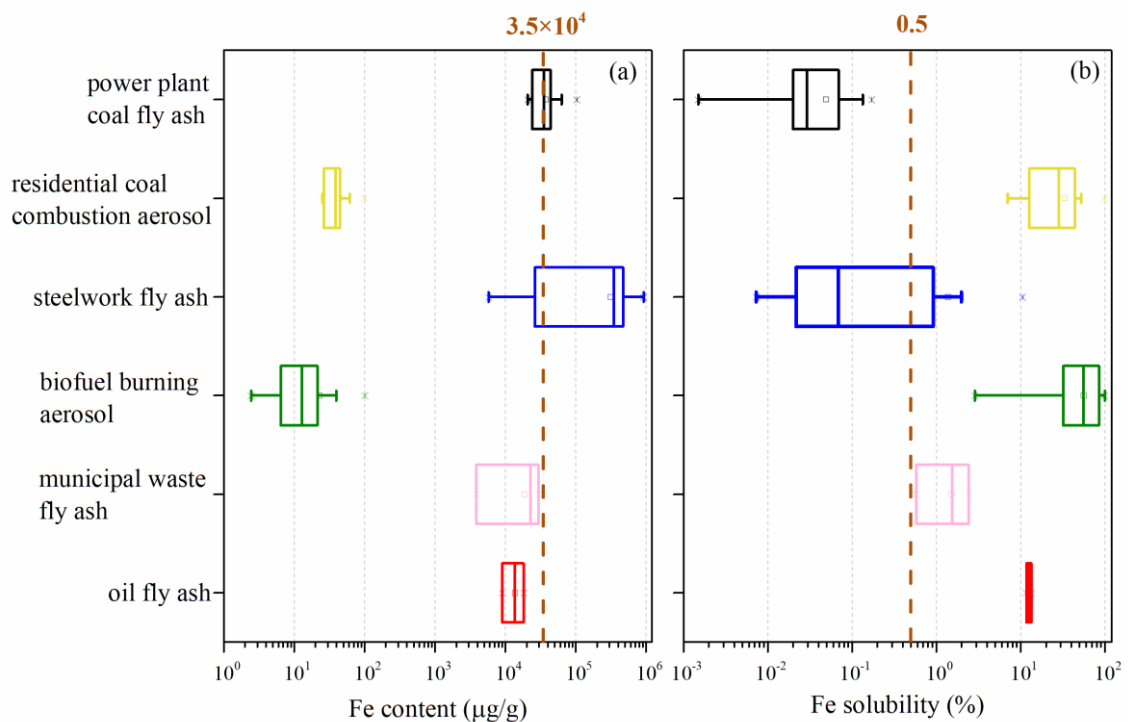
488 Our work considered biofuel burning aerosols for nine types of biofuels, including four
489 types of crop straw, one type of wild grass, and four types of wood. Fe content in biofuel
490 burning aerosols ranged from 0.002 to 0.101 mg/g (Table 2), with average and median values
491 being 0.023 ± 0.026 and 0.013 mg/g, respectively. As shown in Table S6, the average Fe
492 content was determined to be 0.024 ± 0.017 mg/g ($n = 3$) for PM_{2.5} (Patil et al., 2013), very
493 close to our result; in another study (Hildemann et al., 1991), it was determined to be 0.090
494 mg/g for PM₂ ($n = 2$), higher than our result. In some other studies, average Fe content were
495 reported to be in the range of 0.162-0.440 mg/g for PM_{2.5} (Alves et al., 2011; Hedberg et al.,
496 2002; Watson et al., 2001; Zhang et al., 2012) and 0.723 ± 0.661 mg/g for PM₁₀ (Schmidl et
497 al., 2008), much higher than our results.

498 Fe content in biofuel burning aerosols showed large variability in different studies, likely
499 due to variations in combustion conditions and biofuel types. For example, metal content in
500 biofuel burning aerosols depended greatly on biofuel types and regions where biofuel was
501 collected (Goncalves et al., 2010), and aerosol particles emitted by wild grass combustion
502 contained larger amounts of metal than wood combustion (Jahn et al., 2021). Modeling studies
503 have used a similar distribution of Fe content between 0.2 and 0.580 mg/g for biofuel burning
504 aerosols (Luo et al., 2008; Rathod et al., 2020).

505 **3.1.5 Fe contents: comparison of anthropogenic and dust Fe**

506 Figure 2a displays Fe content for anthropogenic particles examined in our current study,
507 and the brown dashed line represents the average Fe content of desert dust (35 mg/g) (Taylor
508 and Mclennan, 1995). Steelwork fly ash has very high Fe content (median: 346.5 mg/g), about

509 one order of magnitude higher than desert dust. Power plant coal fly ash (median: 35.0 mg/g)
 510 has similar Fe content to desert dust. Compared to desert dust, Fe content were around three
 511 orders of magnitude lower for residential coal and biofuel burning aerosol (median: 0.038 and
 512 0.013 mg/g, respectively). The Fe content was much lower for residential coal and biofuel
 513 burning aerosol, likely due to lower combustion temperatures. When combustion occurs at
 514 lower temperature, the carbon content of emitted particles is higher; in addition, lower
 515 combustion temperature is not sufficient to enable Fe in the fuel to enter emitted particles via
 516 volatilization-condensation processes.



517
 518 **Figure 2.** Fe content (a) and solubility (b) measured in our work for power plant coal fly ash,
 519 residential coal combustion aerosol, steelwork fly ash, biofuel burning aerosol, municipal
 520 waste fly ash and oil fly ash. The two brown dash lines represent (a) the Fe content (3.5×10^4
 521 $\mu\text{g/g}$) and (b) Fe solubility ($\sim 0.5\%$) for desert dust, respectively.

522 **3.2 Fe solubility by fuel type**

523 **3.2.1 Power plant coal fly ash**

524 Fe solubility in acetate buffer (pH: 4.3) ranged from 0.002% to 0.17% for power plant
525 coal fly ash (Table 2), with the average and median values being $0.05 \pm 0.05\%$ and 0.03%,
526 respectively. A few previous studies measured Fe solubility of power plant coal fly ash in
527 weakly acidic or circumneutral solutions (Table S7). For example, Fe solubility was measured
528 to be 0.06% in deionized water (Oakes et al., 2012), similar to our result; it was measured to
529 be 0.2% in dilute sulfuric acid solution (pH: 4.7) (Desboeufs et al., 2005), slightly higher than
530 our result; the median Fe solubility was determined to be 0.13% in acetate buffer (pH: 4.3) and
531 0.06% in deionized water (Li et al., 2022b), both higher than the median value we obtained.
532 Overall, our work and previous studies suggest that Fe solubility is low in weakly acidic and
533 circumneutral solutions for power plant coal fly ash, with mean or median values around 0.1%.

534 Some studies also measured Fe solubility of power plant coal fly ash in highly acidic
535 solutions and found them to be much higher than those in weakly acidic and circumneutral
536 solutions. For example, Fe solubilities were found to be in the range of 20-25% at pH of 1-2
537 (Chen et al., 2012), 4.2-8.3% at pH of 2 (Fu et al., 2012), and >40% at pH of 2.1 (Baldo et al.,
538 2022). Although Fe solubility measured in strongly acidic solutions may not reflect initial Fe
539 solubility, these studies suggested that acid processing in the emission plume or wider
540 atmosphere could greatly increase Fe solubility for power plant coal fly ash.

541 **3.2.2 Residential coal combustion aerosol**

542 Fe solubility in acetate buffer (pH: 4.3) was determined to range from 7.03% to 100% for
543 residential coal combustion aerosol (Table 2), with the average and median values being 33.30

544 $\pm 27.71\%$ and 28.45% , respectively. To our knowledge, no previous study has measured Fe
545 solubility for residential coal combustion aerosol. Compared to power plant coal fly ash, Fe
546 solubility was much higher for residential coal combustion aerosol, and such difference can be
547 attributed to much higher temperature in power plant coal combustion than residential coal
548 combustion. Pyrite (FeS_2) is the major Fe-containing mineral in coal (Deng et al., 2015;
549 Oliveira et al., 2016; Rathod et al., 2020). In low-temperature combustion, pyrite is mainly
550 transformed to Fe sulfate (Bhargava et al., 2009) which has very high Fe solubility; as the
551 temperature increases to $>1000\text{ K}$, Fe sulfate is further transformed to hematite and magnetite
552 which exhibit very low solubility (Hu et al., 2006; Ram et al., 1995; Rathod et al., 2020). A
553 previous study (Rathod et al., 2020) used the relationship between combustion temperature and
554 Fe mineralogy in emitted particles to estimate Fe solubility for different combustion aerosols,
555 and Fe solubility was estimated to be as high as $\sim 32.5\%$ for residential coal combustion
556 aerosols, in good agreement with our experimental results.

557 **3.2.3 Steelwork fly ash**

558 Fe solubility in acetate buffer (pH: 4.3) was determined to range from 0.01% to 10.64%
559 for steelwork fly ash (Table 2), and the average and median values were $1.37 \pm 2.77\%$ and
560 0.07% , respectively. We note that Fe solubility was significantly higher (0.92% - 8.59%) for 8
561 samples and very low ($<0.5\%$) for the other 21 samples (Table S3), most of which showed Fe
562 solubility below 0.1% . No previous work has measured Fe solubility for steelwork fly ash. Our
563 experimental results were supported by a modeling study (Rathod et al., 2020) which suggested
564 that the major Fe-containing species in steelwork fly ash were Fe oxides with very low Fe
565 solubilities.

566 **3.2.4 Biofuel burning aerosol**

567 For biofuel burning aerosol, Fe solubility in acetate buffer (pH: 4.3) ranges from 2.86%
568 to 100% with average and median values of $56.07 \pm 30.95\%$ and 55.87%, respectively (Table
569 2). Based on the relationship between combustion temperature and Fe-containing species in
570 emitted aerosols, Fe solubility was previously estimated at 35% for wood burning (i.e., biofuel)
571 aerosol (Rathod et al., 2020), in good agreement with our experimental results.

572 The biofuel examined in our experiment was burnt in a sealed stove and contained no
573 apparent local soil contamination. As such, these results are most representative of domestic
574 biofuel combustion for which the influence of soil-derived Fe can be expected to be negligible.
575 In contrast, wildfires represent dynamic open fire systems that emit aerosol Fe in both fine and
576 coarse fractions (Hamilton et al., 2019). During wildfire combustion, not only is the biofuel
577 (biomass) consumed, but local soils are also entrained into the smoke plumes (Hamilton et al.,
578 2022; Tegler et al., 2023). These soil-derived particles are typically larger (in particle size) and
579 less soluble than their biofuel-derived counterparts (Hamilton et al., 2022), resulting in a larger
580 mass of emitted Fe, albeit with a lower overall Fe solubility. Future studies would benefit from
581 capturing emissions from open burning scenarios to better characterize the properties of
582 wildfire-emitted Fe.

583 **3.2.5 Fe solubilities: comparison of anthropogenic and dust Fe**

584 Figure 2b compares our measured Fe solubility for six types of combustion and
585 anthropogenic particles with that for desert dust. Biofuel burning aerosols (median: 55.87%)
586 and residential coal combustion aerosols (median: 28.45%) exhibited very high Fe solubility.
587 Compared to desert dust, for which Fe solubility is around 0.5% (Chuang et al., 2005; Li et al.,

588 2022b; Ooki et al., 2009; Schroth et al., 2009; Shi et al., 2011), Fe solubility was lower for
589 steelwork fly ash (median: 0.07%) and power plant coal fly ash (median: 0.03%).

590 Overall, Fe solubility in emitted particles was significantly higher for low-temperature
591 combustion (residential and biofuel burning aerosols) than high-temperature combustion
592 (steelwork fly ash and power plant coal fly ash). This is because Fe in emitted particles is
593 mainly highly soluble Fe sulfates for low temperature combustion (Bhargava et al., 2009;
594 Rathod et al., 2020) but Fe oxides with very low solubility for high temperature combustion
595 (Hu et al., 2006; Ram et al., 1995; Rathod et al., 2020).

596 **3.3 Modeling Results**

597 Leveraging new measurements of combustion Fe solubility in residential fuel sources as
598 reported in Sections 3.1 and 3.2, we performed a series of Earth System Model (MIMI)
599 simulations that examined global Fe fluxes in response to modifying anthropogenic Fe
600 solubility parameters at their point of emission. To pair observed solubilities (Table 2) with
601 fuel-types represented in the model, we updated Fe solubility in residential coal burning aerosol
602 from 0.2 to 33% and in residential biofuel burning aerosol from 10 to 56% at the point of
603 emission (Table 3) in both the fine and coarse modes. Smelting Fe solubility was kept at 0.03%
604 for all simulations, since new data did not suggest an alternative solubility from what is
605 currently used (Table 3). We ran one additional simulation with updates to industrial sources
606 (PD-IND: industrial coal Fe solubility from 0.2 to 0.05% and oil from 38 to 25%), but observed
607 impacts to global soluble Fe fluxes following these changes were minimal and are accordingly
608 deferred to the Supplement. A description of the fractional solubilities applied to each
609 anthropogenic fuel type within each model simulation is provided in Table 3.

610

611 **Table 3.** Fractional Fe solubilities applied in each model simulation to reflect experimental
 612 findings. Bolded rows indicate baseline simulations with no changes made to Fe solubility from
 613 previous work using MIMI. To underscore modifications between simulations, a dash (–) is
 614 provided where assigned solubility did not differ from the PD-BASE simulation.

| Simulation | Fe solubility modifications by fuel-type (%) | | | | |
|------------------------|----------------------------------------------|------------------|-----------|---------------------|--------------|
| | Industrial Coal | Residential Coal | Oil | Residential Biofuel | Smelting |
| PD-BASE | 0.2 | 0.2 | 38 | 10 | 0.003 |
| PD-RESI | - | 33 | - | - | - |
| PD-BIOF | - | 33 | - | 56 | - |
| PD-IND | 0.05 | 33 | 25 | 56 | - |
| PI-BASE | NA | NA | NA | 10 | NA |
| PI-BIOF | NA | NA | NA | 56 | NA |
| MID-SSP370-BASE | 0.2 | 0.2 | 38 | 10 | 0.003 |
| MID-SSP370-BIOF | - | 33 | - | 56 | 0.003 |
| END-SSP370-BASE | 0.2 | 0.2 | 38 | 10 | 0.003 |
| END-SSP370-BIOF | - | 33 | - | 56 | 0.003 |

615

616 3.3.1 Impacts on global soluble Fe distribution

617 By applying two new emissions inventories and new solubility parameters for residential
 618 Fe emissions within MIMI, we report a new range of soluble Fe fluxes to the ocean with
 619 regional variations. To isolate the impacts of modifications to each fuel-source, we compared
 620 each model case. When comparing PD-BASE to PD-RESI, the emissions inventory had the
 621 greatest influence on the result per sizeable differences in residential coal emissions by mass.
 622 In the high-residential inventory, global Fe emissions from residential coal were 460 Gg a⁻¹,
 623 exceeding individual emissions from all other fuel types (industrial coal: 310 Gg a⁻¹; oil: 34 Gg
 624 a⁻¹; residential biofuel: 72 Gg a⁻¹) except for smelting (1350 Gg a⁻¹; Table S8). Whereas, in the
 625 low-residential inventory, emissions were nearly two orders of magnitude less at 16 Gg a⁻¹

626 (Table S9), and lower than any other fuel source. Constraining the Fe content in residential
 627 emissions is therefore a more critical knowledge gap to be addressed than constraining the
 628 fractional solubility of this source.

629 Accordingly, when applying the low-residential emissions inventory and using the PD-
 630 RESI solubility parameters, soluble Fe fluxes to the global ocean only increased by $< 1 \text{ Gg a}^{-1}$
 631 (Figure 3; Table 4). Conversely, when applying the high-residential inventory, we saw a 92%
 632 increase in anthropogenic soluble Fe fluxes ($+ 33 \text{ Gg a}^{-1}$) to the ocean, translating to a 7%
 633 increase in overall soluble Fe fluxes including those from dust and wildfire (Figure 3; Table 4).
 634 While the high-residential emissions inventory likely overstates residential coal burning
 635 emissions by Fe mass content, the ocean regions most influenced by residential coal burning
 636 become apparent, facilitating future research locations of highest interest. Anthropogenic
 637 soluble Fe delivery to the Indian Ocean, eastern North Pacific, and parts of the Southern Ocean
 638 increased by 300% to 400%, corresponding with a large increases in emissions from China,
 639 India, Australia, and South Africa (Figure 3). This follows previous reports of relatively large
 640 anthropogenic signals from these regions when compared to global averages (Rathod et al.,
 641 2024; Wang et al., 2015).

642

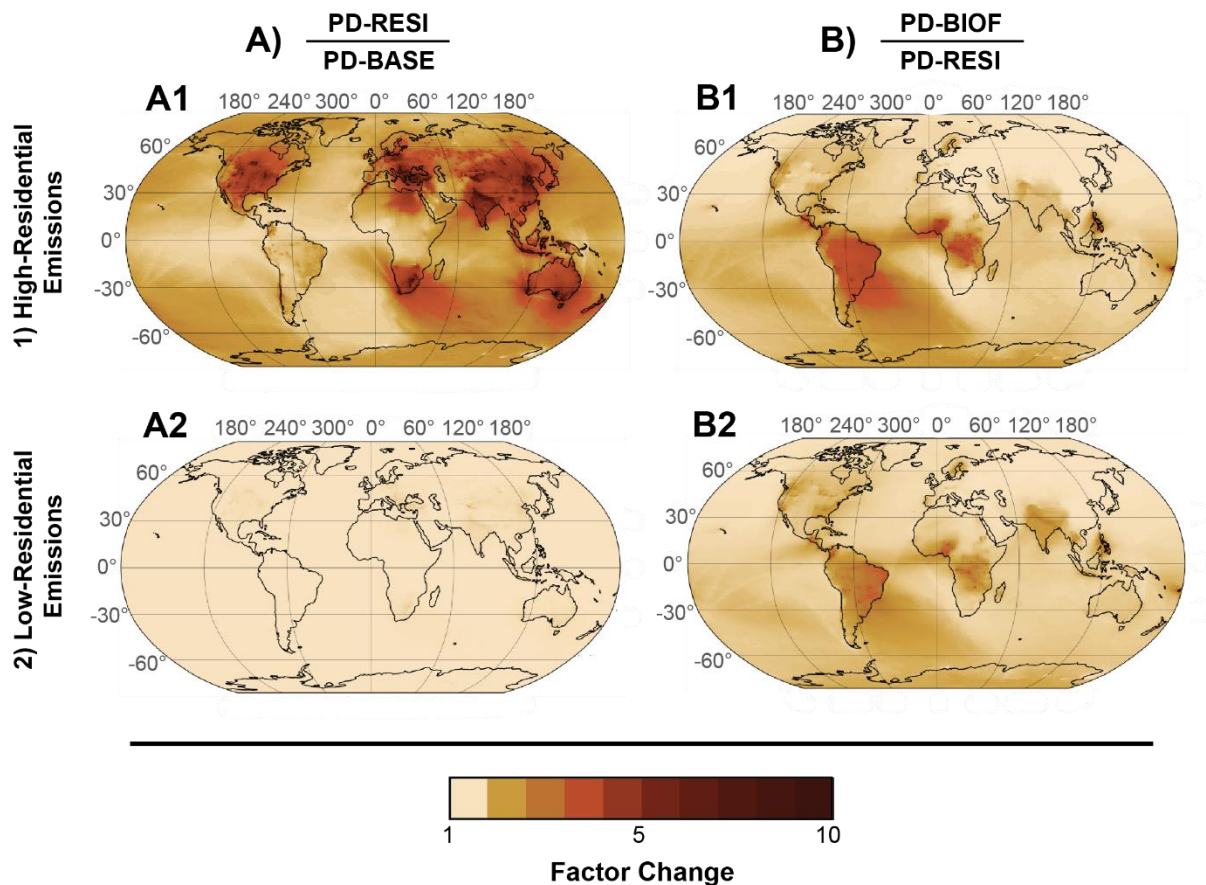
643 **Table 4.** Global soluble Fe deposition fluxes in Gg a^{-1} (relative contribution in %) to ocean
 644 ecosystems for dust, wildfire, and anthropogenic combustion sources in the PD as simulated
 645 by MIMI. Where ranges are reported, they reflect use of the low/high-residential emissions
 646 inventories. Regional fluxes are reported in the Supplement (Table S10).

| Model Simulation (case) | Dust | Wildfire | Anthropogenic Combustion | All Sources |
|-------------------------|------|----------|--------------------------|-------------|
|-------------------------|------|----------|--------------------------|-------------|

| | | | | |
|---------|------------------|---------------|--------------------|-------------------|
| PD-BASE | 305 (83 %) | 26 (7 %) | 36 (10 %) | 367 (100%) |
| PD-RESI | 305 (76-83 %) | 26 (6-7 %) | 37-70 (10-17 %) | 368-401 (100%) |
| PD-BIOF | 305 (74-80 %) | 26 (6-7 %) | 49-81 (13-20 %) | 379-412 (100%) |

647

648 Despite large differences in residential coal emissions between our high- and low-
649 residential inventories, residential biofuel emissions by mass were identical between
650 inventories (72 Gg a⁻¹) because wood burning was already an isolated fuel source in our
651 inventory (Rathod et al., 2020). When using the high-residential inventory, impacts to soluble
652 Fe fluxes by biofuel were largely overshadowed by residential coal, but using the low-
653 inventory, changes to biofuel parameters in the model controlled increases in soluble Fe fluxes.
654 When we increased biofuel Fe solubility (PD-BIOF), soluble Fe fluxes to the ocean increased
655 by an additional 11 Gg a⁻¹, for a total increase of 13-44 Gg a⁻¹ from residential sources (coal +
656 biofuel) when compared to PD-BASE (Table 5). Changes to soluble Fe fluxes from biofuel
657 burning were most concentrated across the South Atlantic (Figure 3), likely due to the long
658 range transport of emissions from the Amazon rainforest and across the Congo River basin
659 where biofuel-burning in cook stoves is a common residential practice (García-López et al.,
660 2025; Stoner et al., 2021). We report a maximum change in soluble Fe fluxes using the high-
661 residential emissions inventory and PD-BIOF solubility parameters, with deposition to the
662 ocean doubling from 40 to 80 Gg a⁻¹ at the global scale (relative to PD-BASE; Table 5).



663

664 **Figure 3.** Relative changes to soluble Fe deposition fluxes using different 1-2) emission
 665 inventories and following modifications to A-B) Fe solubility parameters.

666

667 With soluble dust-Fe (310 Gg a^{-1}) and wildfire-Fe (30 Gg a^{-1}) fluxes, our different
 668 anthropogenic cases (an additional $40\text{-}80 \text{ Gg a}^{-1}$; Table 5) suggest that total soluble Fe fluxes
 669 to the ocean fall between 370 Gg a^{-1} (PD-BASE, both inventories) and 410 Gg a^{-1} (PI-BIOF,
 670 high-residential emissions inventory) at the global scale. These values fall within previous
 671 ranges of uncertainty as reported for Fe deposition fluxes to the ocean (Hamilton et al., 2023;
 672 Ito and Miyakawa, 2023), suggesting that solubility modifications tested herein align with
 673 previous Fe constraints within Earth System Models.

674

675 **Table 5.** Global anthropogenic combustion Fe emission and deposition fluxes (Gg a^{-1}) in the
676 preindustrial (PI), present day (PD), and Future (FU), as simulated by MIMI to two significant
677 figures. Where ranges are reported reflect use of the low/high-residential emissions inventories.

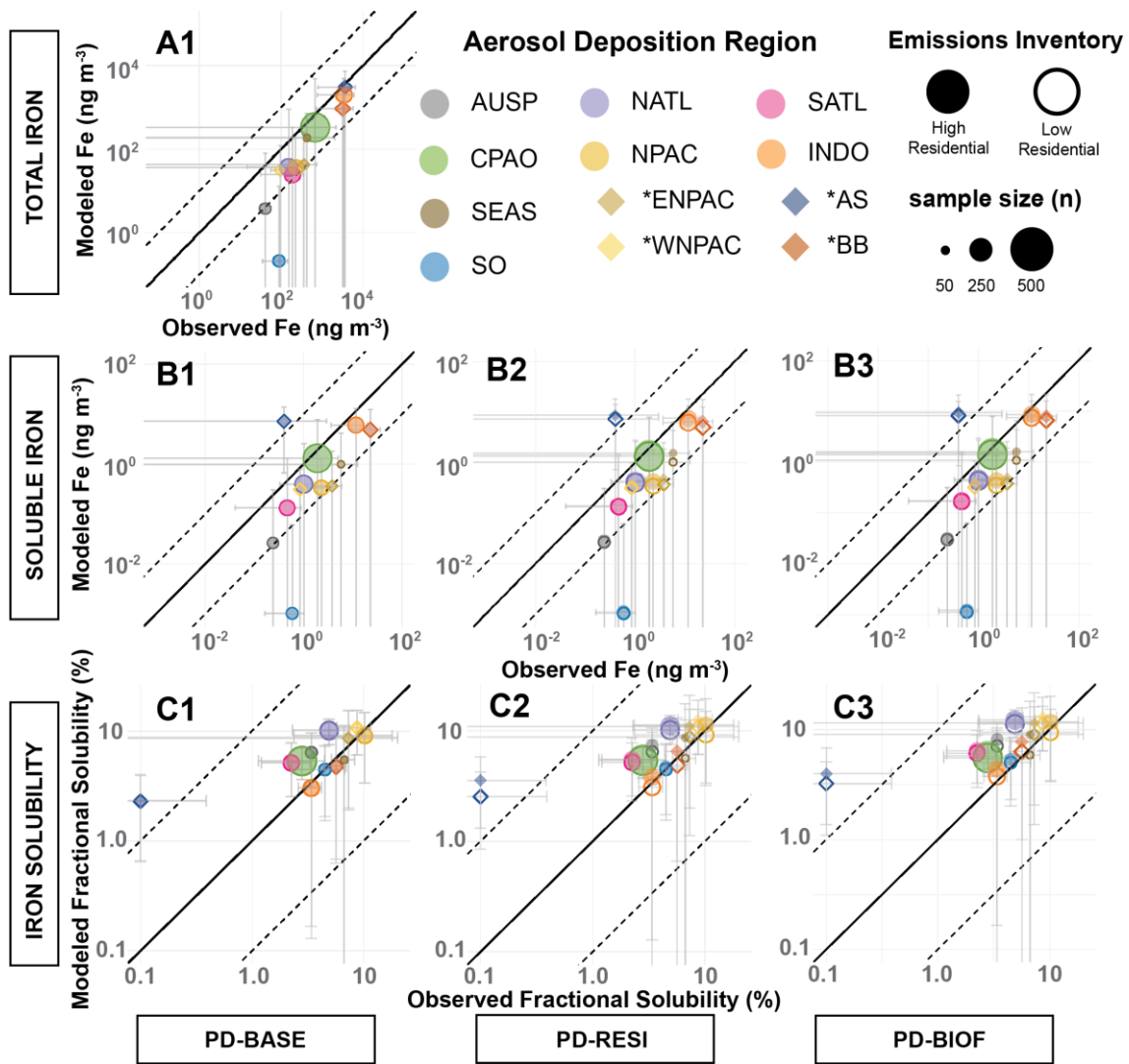
| Emission Scenario | Model Simulation (case) | Fe Content | Global Emission | Global Deposition | Deposition to Ocean |
|-------------------|-------------------------|--------------------|------------------|-------------------|---------------------|
| PI (1750 CE) | PI-BASE | Total (Soluble) | 0.80 (0.08) | 0.80 (0.10) | 0.30 (0.04) |
| | PI-BIOF | Total (Soluble) | 0.80 (0.44) | 0.80 (0.50) | 0.30 (0.20) |
| PD (2010 CE) | PD-BASE | Total (Soluble) | 2220 (20) | 2220 (90) | 590 (40) |
| | PD-BIOF | Total (Soluble) | 2220 (60-170) | 2220 (130-270) | 590 (49-81) |
| FU (2050 CE) | MID-SSP370-BASE | Total (Soluble) | 2400 (20) | 2400 (90) | 620 (40) |
| | MID-SSP370-BIOF | Total (Soluble) | 2400 (180) | 2400 (250) | 620 (80) |
| FU (2100 CE) | END-SSP370-BASE | Total (Soluble) | 1970 (20) | 1970 (80) | 510 (30) |
| | END-SSP370-BIOF | Total (Soluble) | 1970 (90) | 1970 (150) | 510 (50) |

678

679 3.3.2 Model-observation comparisons of total and soluble Fe concentrations

680 Comparison of modeled surface concentrations with regionally grouped, ship-based
681 observations revealed generally good agreement between modeled and observed total and
682 soluble aerosol Fe concentrations for all PD simulations (Figure 4). Modeled total Fe
683 concentrations were slightly underpredicted when compared to observed values but remained
684 well within one order of magnitude for each ocean region, with the exception of the Southern
685 Ocean where total Fe was underestimated by several orders of magnitude. This aligns with
686 previous efforts to model global fluxes of total and soluble aerosol Fe using MIMI v1.0 and
687 other Earth System Models (Ito and Miyakawa, 2023; Ito et al., 2019; Liu et al., 2024). Current

688 hypotheses suggest that an Fe source, such as volcanism or mining, is not currently well
 689 represented in models, or alternatively, that limited observations are not representative of Fe
 690 conditions in the airshed of the Southern Ocean (Ito and Miyakawa, 2023; Liu et al., 2024).
 691



692
 693 **Figure 4.** Comparison of modelling and observational data: A) total Fe, B) soluble Fe, and C)
 694 Fe solubility; 1) PD-BASE, 2) PD-RESI, and 3) PD-BIOF. Data were aggregated over time
 695 and space as medians. Solid/hollow markers indicate use of the high/low-residential emissions
 696 inventories, respectively. Error bars represent spatiotemporal variance within each region. The

697 solid black line indicates a 1-to-1 relationship and the dashed lines represent deviation by ± 1
698 order of magnitude. Only PD-BASE is shown for total Fe per consistency between cases.

699

700 In each case, soluble Fe regression analyses followed a similar trend to total Fe, wherein
701 modeled averages were slightly lower than observed values and fell within one order of
702 magnitude, apart from the Southern Ocean and Arabian Sea (Figure 4, Table S12). In the PD-
703 RESI and PD-BIOF cases, soluble Fe concentrations increased at the global scale, but the
704 degree varied by region. At the global scale, enhancing residential Fe emissions generally
705 improved model skill for soluble Fe concentrations (Figure 4), resulting in an average increase
706 to modeled soluble Fe concentrations by $0.5 \pm 0.7 \text{ ng m}^{-3}$ within each ocean region (Table S10).
707 For regions most influenced by residential coal burning, the improvement in model skill was
708 slightly higher using the high-emissions inventory, especially for Southeastern Asia (ΔRMSE
709 -0.5), the Bay of Bengal ($\Delta\text{RMSE} = -5.0$), and the eastern North Pacific (Figure 4; Table S12;
710 $\Delta\text{RMSE} = -0.1$). For biofuel burning Fe, the emissions inventory had no effect, but enhancing
711 Fe solubility most improved model skill within the South Atlantic Ocean (Figure 4, Table S12
712 $\Delta\text{RMSE} = -0.07$). Complete summary statistics conveying impacts to model skill for soluble
713 Fe concentrations simulated in each run are provided in the Supplement (Table S12).

714 While the high-residential emissions inventory slightly improved estimates for soluble Fe
715 concentrations, the low-residential emissions inventory performed better when capturing
716 fractional solubility for regions influenced by residential coal (Figure 4). Despite these
717 noticeable variations between cases, ultimately, Fe solubilities calculated by the model were
718 aligned with observations within ± 1 order of magnitude for every region except for the Arabian

719 Sea wherein solubility was overestimated by 1-2 orders of magnitude (Figure 4). In previous
720 MIMI-validation efforts (Hamilton et al., 2019), observational data from the Arabian Sea and
721 Bay of Bengal were aggregated as the Indian Ocean and this result was not flagged. While both
722 basins receive substantial anthropogenic aerosol from India, dust from the Middle East more
723 strongly influences the Arabian Sea, and the Bay of Bengal is more strongly affected by
724 anthropogenic emissions across Southeastern Asia (Bali et al., 2019; Guieu et al., 2019).

725 In general, we found that regions with higher dust inputs more often overshoot
726 measurements when compared to regions with less dust deposition and higher relative impact
727 by anthropogenic emissions (Figure 4; Table S12). In each of our modified solubility cases
728 (PD-RESI and PD-BIOF), Fe solubility for southeastern Asia, the Bay of Bengal, and the North
729 Pacific increased, but the regions heavily impacted by dust remained relatively unchanged
730 (Figure 4).

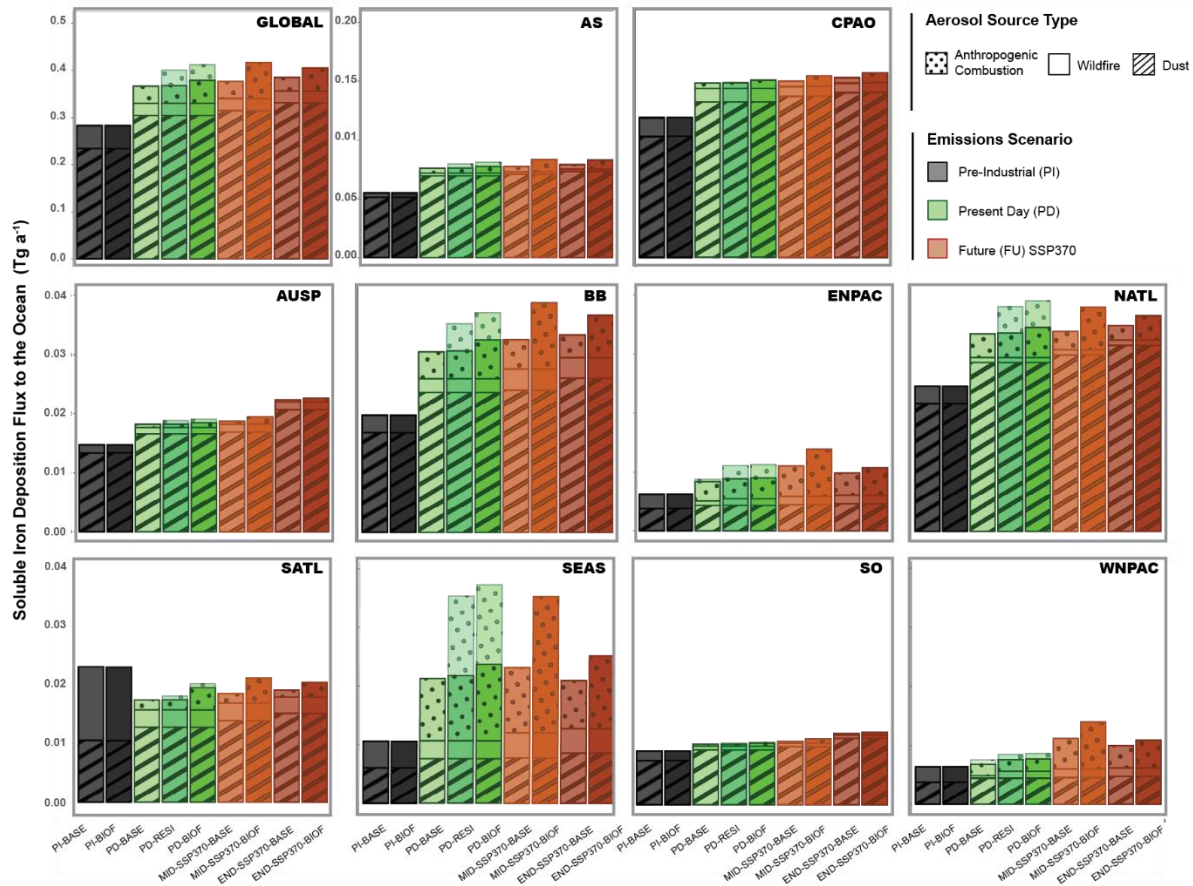
731 Withstanding source-apportioned measurements of residential coal or biofuel aerosol in
732 our observational dataset, we performed additional model-observation comparisons only using
733 measurements collected in ocean regions downwind of strong residential burning influences.
734 These regions were defined as model-resolution grid cells wherein soluble Fe fluxes increased
735 by 100% or more in the PD-BIOF simulations (Figure 3). However, this reduced median-
736 aggregated observational data points from n=990 to n=25, limiting statistical capacity to
737 constrain model fluxes. When using the smaller observational dataset, model-observational
738 comparisons for Total Fe, soluble Fe, and solubility mirrored agreement trends using the larger
739 dataset (Figure 4); those regression analyses are provided in the Supplement (Figures S4-S5)
740 with results from the PD-IND simulation.

741 Although anthropogenic soluble Fe fluxes to marine ecosystems increased by 34% to 123%
742 (<1% to 10% all sources) at the global scale and by 8% to 165% (1% to 21% all sources) for
743 individual regions (Figures 3 and 5), changes to model skill were ultimately modest (Figure 4).
744 The sizeable changes in fluxes with minimal changes to model skill further reinforce the current
745 limitations of ship-based observations in capturing representative soluble Fe fluxes,
746 particularly in the under-sampled Southern Hemisphere and in regions influenced by residential
747 coal and biofuel burning. Future efforts should prioritize expanding the spatial coverage of
748 measurements in these regions to improve model accuracy and understanding of possible
749 anthropogenic influence on remote marine biogeochemistry.

750 **3.3.3 Soluble Fe under PI and FU emission scenarios**

751 PI model simulations serve as a valuable reference point in understanding the specific
752 implications of anthropogenic perturbation to the Earth system. For most regions, soluble Fe
753 fluxes increased between the PI and PD eras (Figure 5), largely attributed to steadily growing
754 anthropogenic combustion emissions and industrial activities over time. Dust and wildfire Fe
755 emissions were also distinct between the PI and PD, due to climatic and land-use change
756 induced feedbacks that have altered global precipitation patterns and dust suspension
757 (Hamilton et al., 2018; Kok et al., 2023; Li et al., 2019; Mahowald et al., 2010). At the global
758 scale, we estimated that current soluble Fe fluxes to marine ecosystems exceed PI fluxes by
759 36-70 Gg a⁻¹, apart from the South Atlantic, wherein soluble Fe fluxes have decreased since
760 the PI era by 2.8-5.6 Gg a⁻¹ (Figure 5). This decrease was likely attributed to reduction in
761 wildfire burned area over past decades, particularly in sub-Saharan Africa (Andela et al., 2017;

762 Jones et al., 2022). Previous work has suggested that wildfire activity during the PI era
 763 exceeded current wildfire regimes at the global scale (Hamilton et al., 2018).



764
 765 **Figure 5.** Deposition fluxes of soluble aerosol Fe to marine ecosystems at the global and
 766 regional scale. Deposition fluxes are source-apportioned (dust, wildfire burning, and
 767 anthropogenic combustion) and provided for each case with distinct solubility parameters. For
 768 the PD, transparent bars represent the high-residential emissions inventory and opaque
 769 represent the low. Conversely, for the FU, only the high-residential inventory was applied, and
 770 the bars are opaque.

771
 772 Regardless of the inventory applied, we observed the largest increases between PI and PD
 773 soluble Fe fluxes in Southeastern Asia, the Bay of Bengal, and the North Atlantic. In

774 Southeastern Asia anthropogenic activity has specifically driven, and is projected to drive,
775 changes to future soluble Fe fluxes (Figure 5). This was the only ocean region wherein
776 anthropogenic sources were comparable (low residential inventory) or exceeded (high
777 residential inventory) dust sources of soluble Fe (Figure 5). When using the high-residential
778 inventory, anthropogenic combustion aerosol constituted up to 72% of all soluble Fe fluxes to
779 marine ecosystems in this region, a 21% increase from PD-BASE. Although dust was still the
780 largest source of Fe to the Bay of Bengal and North Atlantic, anthropogenic combustion also
781 strongly influenced soluble Fe delivery in these regions (Figure 5). When using the high-
782 residential emissions inventory with the -BIOF solubility parameters, the relative contribution
783 by anthropogenic emissions doubled in these regions (Table S10).

784 The inventory and solubility parameters used in each case revealed important implications
785 for projected trends of soluble Fe fluxes moving into the second half of the 21st century. Under
786 the SSP370 FU emissions scenario, anthropogenic Fe fluxes were projected to reach their
787 maxima by 2050 for most deposition regions and then decrease to values at or below current
788 PD conditions by 2100 (Figure 5). However, this trend did not hold for regions within the
789 Southern Hemisphere (Australia/South Pacific, Central Pacific/Atlantic, and Southern Ocean)
790 where soluble aerosol Fe fluxes were projected to continually increase through the end of the
791 century (Figure 5). This was not due to direct changes in anthropogenic combustion emissions,
792 but rather due to changes in dust emissions as the primary source of soluble Fe to the Southern
793 Hemisphere (Figure 5).

794 By the end of the century under SSP370, PD-BASE simulations suggest that soluble Fe
795 deposition to global marine systems will increase slightly from 367 to 369 Gg a⁻¹ (~1% increase)

796 by 2100. However, when considering higher residential Fe emissions with higher solubilities
797 representing new upper bound, projected changes to soluble Fe fluxes between PD/MID-
798 SSP370 and MID-SSP370/END-SSP370 was reversed at the global scale and for many regions,
799 with projected decreases by the end of the century (~2% decrease; Figure 5). The projected
800 losses in soluble Fe between the middle and end of the 21st century was especially apparent for
801 the Bay of Bengal (2-6%), the eastern and western North Pacific (12-29%), and across
802 Southeastern Asia (11-41%) (Figure 5), suggesting that various marine ecosystems could face
803 a more significant deviation from current soluble Fe supply than has previously been
804 represented in Earth System Models.

805 Projected changes in soluble Fe fluxes by 2100 under FU emission scenarios, including
806 SSP370, have strong implications for the spatiotemporal distribution of net marine primary
807 productivity, mostly in Fe limited regions. For example, although we demonstrated that
808 anthropogenic emissions most greatly influenced Fe dynamics across Southeastern Asia, it is
809 important to note that primary production in this ocean region is not typically limited by Fe
810 (Bazzani et al., 2023), so ecosystem-level effects by atmospheric Fe are less likely to be
811 observed therein. However, similar to Southeastern Asia, we found that changes to
812 anthropogenic emissions more strongly impacted soluble Fe fluxes in the eastern North Pacific
813 when compared to dust and wildfire sources. Recent work suggests that the atmospheric supply
814 of anthropogenic Fe has already shifted phytoplankton bloom dynamics in the open ocean by
815 accelerating the seasonal uptake of upwelled nitrogen in HNLC regions, including North
816 Pacific (Hawco et al., 2025). Such regions are anticipated to be especially sensitive to changes

817 in anthropogenic Fe given that they are historically limited by trace metals including Fe
818 (Bazzani et al., 2023; Moore et al., 2013; Nishioka and Obata, 2017).

819 In addition to our findings, diverse lines of evidence suggest that half of the soluble Fe
820 flux to the North Pacific comes from Asian anthropogenic sources (Hamilton et al., 2019;
821 Hamilton et al., 2020a; Hawco et al., 2025; Rathod et al., 2020). Li et al. (2024) found that the
822 magnitude of chlorophyll-a response to Fe deposition off the coast of China was lowered by a
823 factor of 4 during COVID-19 in March 2020 when anthropogenic emissions across East Asia
824 were substantially reduced. The authors speculated that a reduction in soluble Fe from
825 anthropogenic activities, either via the primary emission of soluble Fe or via a reduction in Fe
826 solubilization via co-emitted acidic species (e.g., SO_x), resulted in a lessened supply of soluble
827 Fe delivered during the deposition event. Moreover, using Fe isotopes to trace source origins
828 of atmospheric Fe, Hawco et al. (2025) recently showed that the springtime delivery of
829 anthropogenic Fe could be one major factor driving observed seasonal and geographic shifts to
830 the North Pacific transition zone, a highly productive boundary in the North Pacific. Isotopic
831 signatures capable of distinguishing residential coal combustion from other anthropogenic
832 combustion sources have not yet been identified, but our findings suggest that residential coal
833 burning is an especially important source of soluble Fe to the North Pacific and the South China
834 Sea, and across southeastern Asia. Accordingly, we find that projected losses of anthropogenic
835 emissions over the course of this century will most greatly influence nutrient dynamics in these
836 key marine ecosystems.

837 **4 Conclusions**

838 Anthropogenic activity has added a multitude of new aerosol Fe sources to the atmosphere.
839 Understanding how these new sources alter the magnitude and timing of soluble Fe aerosol
840 fluxes to the ocean aids understanding of how human activity is changing marine primary
841 productivity and ocean ecosystem functions within the Anthropocene. However, estimating the
842 contribution of anthropogenic emissions to soluble aerosol Fe fluxes is challenging given the
843 wide variety of sources, each with their own distinct physicochemical profiles. Lack of
844 observational constraints leads to large variation across different modeling studies on the
845 magnitude of the deposition flux from anthropogenic sources. We address some of these
846 uncertainties in this study by measuring the Fe content and solubility of aerosol Fe from several
847 important anthropogenic sources, including a first assessment of the contribution from two
848 major biofuels, namely residential coal and wood. We find that median Fe solubilities vary by
849 greater than three orders of magnitude across fuel types, from 0.03% for power plant coal fly
850 ash to 55.87% for biofuel burning aerosol.

851 To understand the impact of increasing anthropogenic source representations of fractional
852 Fe solubility, we created two new emission inventories that distinguished residential from
853 industrial sources, and further refined Fe solubility parameters for each sources within MIMI,
854 an atmospheric Fe module embedded within the CESM2.

855 At the global scale, we found that current (PD) soluble Fe fluxes to the ocean from
856 anthropogenic sources could exceed current modeled values by 34% to 123%. This represents
857 an increase of over 3 orders of magnitude from the PI when biofuel sources are assumed to be
858 the only source of anthropogenic Fe (Hamilton et al. 2020a). Projected (FU) soluble Fe fluxes

859 from anthropogenic sources remain similar to the PD through to the middle of the century
860 before declining by up to 38% at the end of the century under SSP370.

861 At the regional scale, including residential coal and biofuel burning sources in the model
862 resulted in the most notable impacts for the Bay of Bengal, across Southeast Asia, and
863 throughout the North Pacific and North Atlantic (i.e., regions strongly influenced by nearby
864 continental anthropogenic activity). However, these regions are generally under-sampled in
865 terms of shipborne aerosol Fe observations, and therefore, to reduce the largest source of
866 uncertainty, more measurements are needed in regions downwind of residential Fe sources to
867 better constrain the contribution of human activity on global biogeochemical cycles.

868

869 **Data availability.**

870 Experimental data can be found in the manuscript or the Supplement, or are available at
871 <https://doi.org/10.5281/zenodo.17766592> (Li, 2025). Modeling output data, coding scripts are
872 available at <https://github.com/haleyplaas/CombustionFe> and emission inventories are located
873 at <https://doi.org/10.5281/zenodo.17903186>.

874 **Competing interests.**

875 At least one of the (co-)authors is a member of the editorial board of Atmospheric
876 Chemistry and Physics.

877 **Author contribution.**

878 MT initiated this study; MT and DSH designed this study and secured funding resources;
879 RL, YZ, YC and TZ conducted experimental work; HEP, SR and DSH conducted modeling
880 work; YY provided key samples used in this work and contributed to data analysis; RL and

881 HEP analyzed the results; RL, HEP, DSH and MT wrote the manuscript; all the authors
882 reviewed and approved the manuscript.

883 **Financial support.**

884 This work was sponsored by National Natural Science Foundation of China (42321003,
885 42507154, 42277088 and 22361162668), International Partnership Program of Chinese
886 Academy of Sciences (164GJHZ2024011FN), Guangzhou Bureau of Science and Technology
887 (2024A04J6533), and Guangdong Foundation for the Program of Science and Technology
888 Research (2023B1212060049).

889

890

891 **References**

- 892 Ahmaruzzaman, M.: A review on the utilization of fly ash, *Progress in Energy and Combustion Science*, 36, 327-
893 363, <https://doi.org/10.1016/j.peccs.2009.11.003>, 2010.
- 894 Al-Abadleh, H. A., Kubicki, J. D., and Meskhidze, N.: A perspective on iron (Fe) in the atmosphere: air quality,
895 climate, and the ocean, *Environmental Science: Processes & Impacts*, 25, 151-164, 10.1039/D2EM00176D,
896 2023.
- 897 Al-Negheimish, A. I., Al-Mutlaq, F. M., Fares, G., Alhozaimy, A. M., and Iqbal Khan, M.: Characterization of
898 chemical accelerators for sustainable recycling of fresh electric-arc furnace dust in cement pastes, *Advanced*
899 *Powder Technology*, 32, 3046-3062, <https://doi.org/10.1016/j.appt.2021.06.019>, 2021.
- 900 Alizadeh, M. and Momeni, M.: The effect of the scrap/DRI ratio on the specification of the EAF dust and its
901 influence on mechanical properties of the concrete treated by its dust, *Construction and Building Materials*,
902 112, 1041-1045, <https://doi.org/10.1016/j.conbuildmat.2016.03.011>, 2016.
- 903 Alsheyab, M. A. T. and Khedaywi, T. S.: Analysis of the Effect of Temperature on the Resilient Modulus of
904 Asphalt Concrete Mixed with Electric Arc Furnace Dust (EAFD), *Water, Air, & Soil Pollution*, 227, 80,
905 10.1007/s11270-016-2776-4, 2016.
- 906 Alves, C., Gonçalves, C., Fernandes, A. P., Tarelho, L., and Pio, C.: Fireplace and woodstove fine particle
907 emissions from combustion of western Mediterranean wood types, *Atmospheric Research*, 101, 692-700,
908 <https://doi.org/10.1016/j.atmosres.2011.04.015>, 2011.
- 909 Andela, N., Morton, D. C., Giglio, L., Chen, Y., van der Werf, G. R., Kasibhatla, P. S., DeFries, R. S., Collatz, G.
910 J., Hantson, S., Kloster, S., Bachelet, D., Forrest, M., Lasslop, G., Li, F., Mangeon, S., Melton, J. R., Yue, C.,
911 and Randerson, J. T.: A human-driven decline in global burned area, *Science*, 356, 1356-1362,
912 10.1126/science.aal4108, 2017.
- 913 Baker, A. R., Li, M., and Chance, R.: Trace Metal Fractional Solubility in Size-Segregated Aerosols From the
914 Tropical Eastern Atlantic Ocean, *Global Biogeochemical Cycles*, 34, e2019GB006510,
915 <https://doi.org/10.1029/2019GB006510>, 2020.
- 916 Baldo, C., Ito, A., Krom, M. D., Li, W., Jones, T., Drake, N., Ignatyev, K., Davidson, N., and Shi, Z.: Iron from
917 coal combustion particles dissolves much faster than mineral dust under simulated atmospheric acidic
918 conditions, *Atmospheric Chemistry and Physics*, 22, 6045-6066, 10.5194/acp-22-6045-2022, 2022.
- 919 Bali, K., Mishra, A. K., Singh, S., Chandra, S., and Lehahn, Y.: Impact of dust storm on phytoplankton bloom
920 over the Arabian Sea: a case study during March 2012, *Environmental science and pollution research*
921 *international*, 26, 11940-11950, 10.1007/s11356-019-04602-7, 2019.
- 922 Bazzani, E., Lauritano, C., and Saggiomo, M.: Southern Ocean Iron Limitation of Primary Production between
923 Past Knowledge and Future Projections, *Journal of Marine Science and Engineering*, 11, 272,
924 <https://doi.org/10.3390/jmse11020272>, 2023.
- 925 Bergas-Massó, E., Gonçalves Ageitos, M., Myriokefalitakis, S., Miller, R. L., van Noije, T., Le Sager, P., Montané
926 Pinto, G., and Pérez García-Pando, C.: Pre-Industrial, Present and Future Atmospheric Soluble Iron
927 Deposition and the Role of Aerosol Acidity and Oxalate Under CMIP6 Emissions, *Earth's Future*, 11,
928 e2022EF003353, <https://doi.org/10.1029/2022EF003353>, 2023.
- 929 Bergas-Masso, E., Hamilton, D. S., Myriokefalitakis, S., Rathod, S., Gonçalves Ageitos, M., and Pérez García-
930 Pando, C.: Future climate-driven fires may boost ocean productivity in the iron-limited North Atlantic, *Nature*
931 *Climate Change*, 15, 784-792, 10.1038/s41558-025-02356-4, 2025.
- 932 Bhargava, S. K., Garg, A., and Subasinghe, N. D.: In situ high-temperature phase transformation studies on pyrite,
933 *Fuel*, 88, 988-993, <https://doi.org/10.1016/j.fuel.2008.12.005>, 2009.

934 Blissett, R. S. and Rowson, N. A.: A review of the multi-component utilisation of coal fly ash, *Fuel*, 97, 1-23,
935 <https://doi.org/10.1016/j.fuel.2012.03.024>, 2012.

936 Bond, T. C., Streets, D. G., Yarber, K. F., Nelson, S. M., Woo, J.-H., and Klimont, Z.: A technology-based global
937 inventory of black and organic carbon emissions from combustion, *Journal of Geophysical Research:*
938 *Atmospheres*, 109, <https://doi.org/10.1029/2003JD003697>, 2004.

939 Bond, T. C., Bhardwaj, E., Dong, R., Jogani, R., Jung, S., Roden, C., Streets, D. G., and Trautmann, N. M.:
940 Historical emissions of black and organic carbon aerosol from energy-related combustion, 1850–2000, *Global*
941 *Biogeochemical Cycles*, 21, <https://doi.org/10.1029/2006GB002840>, 2007.

942 Chen, H., Laskin, A., Baltrusaitis, J., Gorski, C. A., Scherer, M. M., and Grassian, V. H.: Coal Fly Ash as a Source
943 of Iron in Atmospheric Dust, *Environmental Science & Technology*, 46, 2112-2120, 2012.

944 Chen, Y., Wang, Z., Fang, Z., Huang, C., Xu, H., Zhang, H., Zhang, T., Wang, F., Luo, L., Shi, G., Wang, X., and
945 Tang, M.: Dominant Contribution of Non-dust Primary Emissions and Secondary Processes to Dissolved
946 Aerosol Iron, *Environmental Science & Technology*, 58, 17355-17363, [10.1021/acs.est.4c05816](https://doi.org/10.1021/acs.est.4c05816), 2024.

947 Chuang, P. Y., Duvall, R. M., Shafer, M. M., and Schauer, J. J.: The origin of water soluble particulate iron in the
948 Asian atmospheric outflow, *Geophys. Res. Lett.*, 32, 4, [10.1029/2004gl021946](https://doi.org/10.1029/2004gl021946), 2005.

949 Danabasoglu, G., Lamarque, J. F., Bacmeister, J., Bailey, D. A., DuVivier, A. K., Edwards, J., Emmons, L. K.,
950 Fasullo, J., Garcia, R., Gettelman, A., Hannay, C., Holland, M. M., Large, W. G., Lauritzen, P. H., Lawrence,
951 D. M., Lenaerts, J. T. M., Lindsay, K., Lipscomb, W. H., Mills, M. J., Neale, R., Oleson, K. W., Otto-Bliesner,
952 B., Phillips, A. S., Sacks, W., Tilmes, S., van Kampenhou, L., Vertenstein, M., Bertini, A., Dennis, J., Deser,
953 C., Fischer, C., Fox-Kemper, B., Kay, J. E., Kinnison, D., Kushner, P. J., Larson, V. E., Long, M. C., Mickelson,
954 S., Moore, J. K., Nienhouse, E., Polvani, L., Rasch, P. J., and Strand, W. G.: The Community Earth System
955 Model Version 2 (CESM2), *Journal of Advances in Modeling Earth Systems*, 12, e2019MS001916,
956 <https://doi.org/10.1029/2019MS001916>, 2020.

957 Deng, J., Ma, X., Zhang, Y., Li, Y., and Zhu, W.: Effects of pyrite on the spontaneous combustion of coal,
958 *International Journal of Coal Science & Technology*, 2, 306-311, [10.1007/s40789-015-0085-y](https://doi.org/10.1007/s40789-015-0085-y), 2015.

959 Desboeufs, K., Formenti, P., Torres-Sánchez, R., Schepanski, K., Chaboureaud, J. P., Andersen, H., Cermak, J.,
960 Feuerstein, S., Laurent, B., Klopffer, D., Namwoonde, A., Cazaunau, M., Chevaillier, S., Feron, A., Mirande-
961 Bret, C., Triquet, S., and Piketh, S. J.: Fractional solubility of iron in mineral dust aerosols over coastal
962 Namibia: a link to marine biogenic emissions?, *Atmos. Chem. Phys.*, 24, 1525-1541, [10.5194/acp-24-1525-](https://doi.org/10.5194/acp-24-1525-2024)
963 [2024](https://doi.org/10.5194/acp-24-1525-2024), 2024.

964 Desboeufs, K. V., Sofikitis, A., Losno, R., Colin, J. L., and Ausset, P.: Dissolution and solubility of trace metals
965 from natural and anthropogenic aerosol particulate matter, *Chemosphere*, 58, 195-203,
966 <https://doi.org/10.1016/j.chemosphere.2004.02.025>, 2005.

967 Dutta, B. K., Khanra, S., and Mallick, D.: Leaching of elements from coal fly ash: Assessment of its potential for
968 use in filling abandoned coal mines, *Fuel*, 88, 1314-1323, 2009.

969 Elliott, H. E., Pependorf, K. J., Blades, E., Royer, H. M., Pollier, C. G. L., Oehlert, A. M., Kukkadapu, R., Ault,
970 A., and Gaston, C. J.: Godzilla mineral dust and La Soufrière volcanic ash fallout immediately stimulate
971 marine microbial phosphate uptake, *Frontiers in Marine Science*, Volume 10 - 2023,
972 [10.3389/fmars.2023.1308689](https://doi.org/10.3389/fmars.2023.1308689), 2024.

973 Fu, H., Lin, J., Shang, G., Dong, W., Grassian, V. H., Carmichael, G. R., Li, Y., and Chen, J.: Solubility of Iron
974 from Combustion Source Particles in Acidic Media Linked to Iron Speciation, *Environmental Science &*
975 *Technology*, 46, 11119-11127, 2012.

976 García-López, N., Ingabire, A. S., Bailis, R., Eriksson, A. C., Isaxon, C., and Boman, C.: Biomass cookstove
977 emissions—a systematic review on aerosol and particle properties of relevance for health, climate, and the

978 environment, *Environmental Research Letters*, 20, 053002, 10.1088/1748-9326/adc615, 2025.

979 Goncalves, C., Alves, C., Evtyugina, M., Mirante, F., Pio, C., Caseiro, A., Schmidl, C., Bauer, H., and Carvalho,
980 F.: Characterisation of PM10 emissions from woodstove combustion of common woods grown in Portugal,
981 *Atmospheric Environment*, 44, 4474-4480, <https://doi.org/10.1016/j.atmosenv.2010.07.026>, 2010.

982 Goodarzi, F.: Characteristics and composition of fly ash from Canadian coal-fired power plants, *Fuel*, 85, 1418-
983 1427, <https://doi.org/10.1016/j.fuel.2005.11.022>, 2006.

984 Guieu, C., Al Azhar, M., Aumont, O., Mahowald, N., Levy, M., Ethé, C., and Lachkar, Z.: Major Impact of Dust
985 Deposition on the Productivity of the Arabian Sea, *Geophys. Res. Lett.*, 46, 6736-6744,
986 <https://doi.org/10.1029/2019GL082770>, 2019.

987 Hamilton, D., Kasoar, M., Bergas-Massó, E., Dalmonech, D., Hantson, S., Lasslop, G., Voulgarakis, A., and Wells,
988 C.: Global Warming Increases Fire Emissions but Resulting Aerosol Forcing is Uncertain, 10.21203/rs.3.rs-
989 4567012/v1, 2024.

990 Hamilton, D. S., Scanza, R. A., Rathod, S. D., Bond, T. C., Kok, J. F., Li, L., Matsui, H., and Mahowald, N. M.:
991 Recent (1980 to 2015) Trends and Variability in Daily-to-Interannual Soluble Iron Deposition from Dust, Fire,
992 and Anthropogenic Sources, *Geophys. Res. Lett.*, 47, e2020GL089688,
993 <https://doi.org/10.1029/2020GL089688>, 2020a.

994 Hamilton, D. S., Hantson, S., Scott, C. E., Kaplan, J. O., Pringle, K. J., Nieradzik, L. P., Rap, A., Folberth, G. A.,
995 Spracklen, D. V., and Carslaw, K. S.: Reassessment of pre-industrial fire emissions strongly affects
996 anthropogenic aerosol forcing, *Nature Communications*, 9, 3182, 10.1038/s41467-018-05592-9, 2018.

997 Hamilton, D. S., Scanza, R. A., Feng, Y., Guinness, J., Kok, J. F., Li, L., Liu, X., Rathod, S. D., Wan, J. S., Wu,
998 M., and Mahowald, N. M.: Improved methodologies for Earth system modelling of atmospheric soluble iron
999 and observation comparisons using the Mechanism of Intermediate complexity for Modelling Iron (MIMI
1000 v1.0), *Geoscientific Model Development*, 12, 3835-3862, 10.5194/gmd-12-3835-2019, 2019.

1001 Hamilton, D. S., Baker, A. R., Iwamoto, Y., Gassó, S., Bergas-Masso, E., Deutch, S., Dinasquet, J., Kondo, Y.,
1002 Llorc, J., Myriokefalitakis, S., Perron, M. M. G., Wegmann, A., and Yoon, J.-E.: An aerosol odyssey:
1003 Navigating nutrient flux changes to marine ecosystems, *Elementa: Science of the Anthropocene*, 11, 00037,
1004 10.1525/elementa.2023.00037, 2023.

1005 Hamilton, D. S., Moore, J. K., Arneth, A., Bond, T. C., Carslaw, K. S., Hantson, S., Ito, A., Kaplan, J. O., Lindsay,
1006 K., Nieradzik, L., Rathod, S. D., Scanza, R. A., and Mahowald, N. M.: Impact of Changes to the Atmospheric
1007 Soluble Iron Deposition Flux on Ocean Biogeochemical Cycles in the Anthropocene, *Global Biogeochemical*
1008 *Cycles*, 34, e2019GB006448, <https://doi.org/10.1029/2019GB006448>, 2020b.

1009 Hamilton, D. S., Perron, M. M. G., Bond, T. C., Bowie, A. R., Buchholz, R. R., Guieu, C., Ito, A., Maenhaut, W.,
1010 Myriokefalitakis, S., Olgun, N., Rathod, S. D., Schepanski, K., Tagliabue, A., Wagner, R., and Mahowald, N.
1011 M.: Earth, Wind, Fire, and Pollution: Aerosol Nutrient Sources and Impacts on Ocean Biogeochemistry, *Annu.*
1012 *Rev. Mar. Sci.*, 14, 303-330, 10.1146/annurev-marine-031921-013612, 2022.

1013 Hawco, N. J., Conway, T. M., Coesel, S. N., Barone, B., Seelen, E. A., Yang, S.-C., Bundy, R. M., Pinedo-
1014 Gonzalez, P., Bian, X., Sieber, M., Lanning, N. T., Fitzsimmons, J. N., Foreman, R. K., König, D., Groussman,
1015 M. J., Allen, J. G., Juranek, L. W., White, A. E., Karl, D. M., Armbrust, E. V., and John, S. G.: Anthropogenic
1016 iron alters the spring phytoplankton bloom in the North Pacific transition zone, *Proceedings of the National*
1017 *Academy of Sciences*, 122, e2418201122, 10.1073/pnas.2418201122, 2025.

1018 Hedberg, E., Kristensson, A., Ohlsson, M., Johansson, C., Johansson, P.-Å., Swietlicki, E., Vesely, V., Wideqvist,
1019 U., and Westerholm, R.: Chemical and physical characterization of emissions from birch wood combustion in
1020 a wood stove, *Atmospheric Environment*, 36, 4823-4837, [https://doi.org/10.1016/S1352-2310\(02\)00417-X](https://doi.org/10.1016/S1352-2310(02)00417-X),
1021 2002.

1022 Hildemann, L. M., Markowski, G. R., and Cass, G. R.: Chemical composition of emissions from urban sources of
1023 fine organic aerosol, *Environmental Science & Technology*, 25, 744-759, 10.1021/es00016a021, 1991.

1024 Hoesly, R. M., Smith, S. J., Feng, L., Klimont, Z., Janssens-Maenhout, G., Pitkanen, T., Seibert, J. J., Vu, L.,
1025 Andres, R. J., Bolt, R. M., Bond, T. C., Dawidowski, L., Kholod, N., Kurokawa, J. I., Li, M., Liu, L., Lu, Z.,
1026 Moura, M. C. P., O'Rourke, P. R., and Zhang, Q.: Historical (1750–2014) anthropogenic emissions of reactive
1027 gases and aerosols from the Community Emissions Data System (CEDS), *Geoscientific Model Development*,
1028 11, 369-408, 10.5194/gmd-11-369-2018, 2018.

1029 Hu, G., Dam-Johansen, K., Wedel, S., and Hansen, J. P.: Decomposition and oxidation of pyrite, *Progress in*
1030 *Energy and Combustion Science*, 32, 295-314, <https://doi.org/10.1016/j.pecs.2005.11.004>, 2006.

1031 Itahashi, S., Hattori, S., Ito, A., Sadanaga, Y., Yoshida, N., and Matsuki, A.: Role of Dust and Iron Solubility in
1032 Sulfate Formation during the Long-Range Transport in East Asia Evidenced by ¹⁷O-Excess Signatures,
1033 *Environmental Science & Technology*, 56, 13634-13643, 10.1021/acs.est.2c03574, 2022.

1034 Ito, A. and Miyakawa, T.: Aerosol Iron from Metal Production as a Secondary Source of Bioaccessible Iron,
1035 *Environmental Science & Technology*, 57, 4091-4100, 10.1021/acs.est.2c06472, 2023.

1036 Ito, A. and Shi, Z.: Delivery of anthropogenic bioavailable iron from mineral dust and combustion aerosols to the
1037 ocean, *Atmospheric Chemistry and Physics*, 16, 85-99, 10.5194/acp-16-85-2016, 2016.

1038 Ito, A., Lin, G., and Penner, J. E.: Radiative forcing by light-absorbing aerosols of pyrogenetic iron oxides,
1039 *Scientific Reports*, 8, 7347, 10.1038/s41598-018-25756-3, 2018.

1040 Ito, A., Ye, Y., Baldo, C., and Shi, Z.: Ocean fertilization by pyrogenic aerosol iron, *npj Climate and Atmospheric*
1041 *Science*, 4, 30, 10.1038/s41612-021-00185-8, 2021.

1042 Ito, A., Myriokefalitakis, S., Kanakidou, M., Mahowald, N. M., Scanza, R. A., Hamilton, D. S., Baker, A. R.,
1043 Jickells, T., Sarin, M., Bikkina, S., Gao, Y., Shelley, R. U., Buck, C. S., Landing, W. M., Bowie, A. R., Perron,
1044 M. M. G., Guieu, C., Meskhidze, N., Johnson, M. S., Feng, Y., Kok, J. F., Nenes, A., and Duce, R. A.:
1045 Pyrogenic iron: The missing link to high iron solubility in aerosols, *Sci. Adv.*, 5, 10, 10.1126/sciadv.aau7671,
1046 2019.

1047 Jahn, L. G., Jahl, L. G., Bland, G. D., Bowers, B. B., Monroe, L. W., and Sullivan, R. C.: Metallic and Crustal
1048 Elements in Biomass-Burning Aerosol and Ash: Prevalence, Significance, and Similarity to Soil Particles,
1049 *ACS Earth Space Chem.*, 5, 136-148, 10.1021/acsearthspacechem.0c00191, 2021.

1050 Jankowski, J., Ward, C. R., French, D., and Groves, S.: Mobility of trace elements from selected Australian fly
1051 ashes and its potential impact on aquatic ecosystems, *Fuel*, 85, 243-256, 2006.

1052 Johnson, M. S. and Meskhidze, N.: Atmospheric dissolved iron deposition to the global oceans: effects of oxalate-
1053 promoted Fe dissolution, photochemical redox cycling, and dust mineralogy, *Geoscientific Model*
1054 *Development*, 6, 1137-1155, 10.5194/gmd-6-1137-2013, 2013.

1055 Jones, M. W., Abatzoglou, J. T., Veraverbeke, S., Andela, N., Lasslop, G., Forkel, M., Smith, A. J. P., Burton, C.,
1056 Betts, R. A., van der Werf, G. R., Sitch, S., Canadell, J. G., Santín, C., Kolden, C., Doerr, S. H., and Le Quéré,
1057 C.: Global and Regional Trends and Drivers of Fire Under Climate Change, *Reviews of Geophysics*, 60,
1058 e2020RG000726, <https://doi.org/10.1029/2020RG000726>, 2022.

1059 Journet, E., Desboeufs, K. V., Caquineau, S., and Colin, J.-L.: Mineralogy as a critical factor of dust iron solubility,
1060 *Geophys. Res. Lett.*, 35, 10.1029/2007gl031589, 2008.

1061 Kok, J. F., Storelvmo, T., Karydis, V. A., Adebisi, A. A., Mahowald, N. M., Evan, A. T., He, C., and Leung, D.
1062 M.: Mineral dust aerosol impacts on global climate and climate change, *Nature Reviews Earth & Environment*,
1063 4, 71-86, 10.1038/s43017-022-00379-5, 2023.

1064 Kurisu, M., Sakata, K., Uematsu, M., Ito, A., and Takahashi, Y.: Contribution of combustion Fe in marine aerosols
1065 over the northwestern Pacific estimated by Fe stable isotope ratios, *Atmos. Chem. Phys.*, 21, 16027-16050,

1066 10.5194/acp-21-16027-2021, 2021.

1067 Kutchko, B. G. and Kim, A. G.: Fly ash characterization by SEM–EDS, *Fuel*, 85, 2537-2544, 2006.

1068 López-García, P., Gelado-Caballero, M. D., Patey, M. D., and Hernández-Brito, J. J.: Atmospheric fluxes of
1069 soluble nutrients and Fe: More than three years of wet and dry deposition measurements at Gran Canaria
1070 (Canary Islands), *Atmospheric Environment*, 246, 118090, <https://doi.org/10.1016/j.atmosenv.2020.118090>,
1071 2021.

1072 Laforest, G. and Duchesne, J.: Stabilization of electric arc furnace dust by the use of cementitious materials: Ionic
1073 competition and long-term leachability, *Cement and Concrete Research*, 36, 1628-1634,
1074 <https://doi.org/10.1016/j.cemconres.2006.05.012>, 2006.

1075 Li, C., Liu, W., Jiao, F., Yang, C., Li, G., Liu, S., and Qin, W.: Separation and recovery of zinc, lead and iron from
1076 electric arc furnace dust by low temperature smelting, *Separation and Purification Technology*, 312, 123355,
1077 <https://doi.org/10.1016/j.seppur.2023.123355>, 2023.

1078 Li, F., Val Martin, M., Andreae, M. O., Arneth, A., Hantson, S., Kaiser, J. W., Lasslop, G., Yue, C., Bachelet, D.,
1079 Forrest, M., Kluzek, E., Liu, X., Mangeon, S., Melton, J. R., Ward, D. S., Darnenov, A., Hickler, T., Ichoku,
1080 C., Magi, B. I., Sitch, S., van der Werf, G. R., Wiedinmyer, C., and Rabin, S. S.: Historical (1700–2012) global
1081 multi-model estimates of the fire emissions from the Fire Modeling Intercomparison Project (FireMIP),
1082 *Atmospheric Chemistry and Physics*, 19, 12545-12567, 10.5194/acp-19-12545-2019, 2019.

1083 Li, L., Mahowald, N. M., Kok, J. F., Liu, X., Wu, M., Leung, D. M., Hamilton, D. S., Emmons, L. K., Huang, Y.,
1084 Sexton, N., Meng, J., and Wan, J.: Importance of different parameterization changes for the updated dust cycle
1085 modeling in the Community Atmosphere Model (version 6.1), *Geoscientific Model Development*, 15, 8181-
1086 8219, 10.5194/gmd-15-8181-2022, 2022a.

1087 Li, R.: Volume mean diameters of fly ash and bottom ash samples [Data set], Zenodo,
1088 <https://doi.org/10.5281/zenodo.17766592>, 2025.

1089 Li, R., Zhang, H., Wang, F., He, Y., Huang, C., Luo, L., Dong, S., Jia, X., and Tang, M.: Mass fractions, solubility,
1090 speciation and isotopic compositions of iron in coal and municipal waste fly ash, *Science of The Total
1091 Environment*, 838, 155974, <https://doi.org/10.1016/j.scitotenv.2022.155974>, 2022b.

1092 Li, R., Zhang, H., Wang, F., Ren, Y., Jia, S., Jiang, B., Jia, X., Tang, Y., and Tang, M.: Abundance and fractional
1093 solubility of phosphorus and trace metals in combustion ash and desert dust: Implications for bioavailability
1094 and reactivity, *Science of The Total Environment*, 816, 151495,
1095 <https://doi.org/10.1016/j.scitotenv.2021.151495>, 2022c.

1096 Li, S., Zhang, B., Wu, D., Li, Z., Chu, S.-Q., Ding, X., Tang, X., Chen, J., and Li, Q.: Magnetic Particles
1097 Unintentionally Emitted from Anthropogenic Sources: Iron and Steel Plants, *Environmental Science &
1098 Technology Letters*, 8, 295-300, 10.1021/acs.estlett.1c00164, 2021.

1099 Li, W., Xu, L., Liu, X., Zhang, J., Lin, Y., Yao, X., Gao, H., Zhang, D., Chen, J., Wang, W., Harrison, R. M.,
1100 Zhang, X., Shao, L., Fu, P., Nenes, A., and Shi, Z.: Air pollution–aerosol interactions produce more
1101 bioavailable iron for ocean ecosystems, *Sci. Adv.*, 3, e1601749, 10.1126/sciadv.1601749, 2017.

1102 Li, Y., Wang, W., Han, Y., Liu, W., Wang, R., Zhang, R., Zhao, Z., Sheng, L., and Zhou, Y.: Impact of COVID-19
1103 emission reduction on dust aerosols and marine chlorophyll-a concentration, *Science of The Total
1104 Environment*, 918, 170493, <https://doi.org/10.1016/j.scitotenv.2024.170493>, 2024.

1105 Liu, C., Han, G., Hu, B., Geng, F., Liu, M., Dai, S., and Yang, Y.: Fast Screening of Coal Fly Ash with Potential
1106 for Rare Earth Element Recovery by Electron Paramagnetic Resonance Spectroscopy, *Environmental Science
1107 & Technology*, 55, 16716-16722, 10.1021/acs.est.1c06658, 2021.

1108 Liu, L., Li, W., Lin, Q., Wang, Y., Zhang, J., Zhu, Y., Yuan, Q., Zhou, S., Zhang, D., Baldo, C., and Shi, Z.: Size-
1109 dependent aerosol iron solubility in an urban atmosphere, *npj Climate and Atmospheric Science*, 5, 53,

1110 10.1038/s41612-022-00277-z, 2022.

1111 Liu, M., Matsui, H., Hamilton, D. S., Rathod, S. D., Lamb, K. D., and Mahowald, N. M.: Representation of iron
1112 aerosol size distributions of anthropogenic emissions is critical in evaluating atmospheric soluble iron input
1113 to the ocean, *Atmospheric Chemistry and Physics*, 24, 13115-13127, 10.5194/acp-24-13115-2024, 2024.

1114 Loaiza, A., Cifuentes, S., and Colorado, H. A.: Asphalt modified with superfine electric arc furnace steel dust
1115 (EAF dust) with high zinc oxide content, *Construction and Building Materials*, 145, 538-547,
1116 <https://doi.org/10.1016/j.conbuildmat.2017.04.050>, 2017.

1117 Longo, A. F., Feng, Y., Lai, B., Landing, W. M., Shelley, R. U., Nenes, A., Mihalopoulos, N., Violaki, K., and
1118 Ingall, E. D.: Influence of Atmospheric Processes on the Solubility and Composition of Iron in Saharan Dust,
1119 *Environmental Science & Technology*, 50, 6912-6920, 10.1021/acs.est.6b02605, 2016.

1120 Luo, C., Mahowald, N., Bond, T., Chuang, P. Y., Artaxo, P., Siefert, R., Chen, Y., and Schauer, J.: Combustion
1121 iron distribution and deposition, *Global Biogeochemical Cycles*, 22, 10.1029/2007GB002964, 2008.

1122 Machado, J. G. M. S., Brehm, F. A., Moraes, C. A. M., Santos, C. A. d., Vilela, A. C. F., and Cunha, J. B. M. d.:
1123 Chemical, physical, structural and morphological characterization of the electric arc furnace dust, *Journal of*
1124 *hazardous materials*, 136, 953-960, <https://doi.org/10.1016/j.jhazmat.2006.01.044>, 2006.

1125 Mahowald, N. M., Hamilton, D. S., Mackey, K. R. M., Moore, J. K., Baker, A. R., Scanza, R. A., and Zhang, Y.:
1126 Aerosol trace metal leaching and impacts on marine microorganisms, *Nature Communications*, 9, 2614,
1127 10.1038/s41467-018-04970-7, 2018.

1128 Mahowald, N. M., Engelstaedter, S., Luo, C., Sealy, A., Artaxo, P., Benitez-Nelson, C., Bonnet, S., Chen, Y.,
1129 Chuang, P. Y., Cohen, D. D., Dulac, F., Herut, B., Johansen, A. M., Kubilay, N., Losno, R., Maenhaut, W.,
1130 Paytan, A., Prospero, J. M., Shank, L. M., and Siefert, R. L.: Atmospheric Iron Deposition: Global Distribution,
1131 Variability, and Human Perturbations*, *Annu. Rev. Mar. Sci.*, 1, 245-278,
1132 <https://doi.org/10.1146/annurev.marine.010908.163727>, 2009.

1133 Mahowald, N. M., Kloster, S., Engelstaedter, S., Moore, J. K., Mukhopadhyay, S., McConnell, J. R., Albani, S.,
1134 Doney, S. C., Bhattacharya, A., Curran, M. A. J., Flanner, M. G., Hoffman, F. M., Lawrence, D. M., Lindsay,
1135 K., Mayewski, P. A., Neff, J., Rothenberg, D., Thomas, E., Thornton, P. E., and Zender, C. S.: Observed 20th
1136 century desert dust variability: impact on climate and biogeochemistry, *Atmospheric Chemistry and Physics*,
1137 10, 10875-10893, 10.5194/acp-10-10875-2010, 2010.

1138 Marafante, M., Bertinetti, S., Carena, L., Fabbri, D., Malandrino, M., Vione, D., and Berto, S.: Chemical
1139 characterization and speciation of the soluble fraction of Arctic PM10, *Analytical and Bioanalytical Chemistry*,
1140 416, 1389-1398, 10.1007/s00216-024-05131-0, 2024.

1141 Matsui, H., Mahowald, N. M., Moteki, N., Hamilton, D. S., Ohata, S., Yoshida, A., Koike, M., Scanza, R. A., and
1142 Flanner, M. G.: Anthropogenic combustion iron as a complex climate forcer, *Nature Communications*, 9, 1593,
1143 10.1038/s41467-018-03997-0, 2018.

1144 McDaniel, M. F. M., Ingall, E. D., Morton, P. L., Castorina, E., Weber, R. J., Shelley, R. U., Landing, W. M.,
1145 Longo, A. F., Feng, Y., and Lai, B.: Relationship between Atmospheric Aerosol Mineral Surface Area and Iron
1146 Solubility, *ACS Earth Space Chem.*, 3, 2443-2451, 10.1021/acsearthspacechem.9b00152, 2019.

1147 Meij, R.: Trace element behavior in coal-fired power plants, *Fuel Processing Technology*, 39, 199-217,
1148 [https://doi.org/10.1016/0378-3820\(94\)90180-5](https://doi.org/10.1016/0378-3820(94)90180-5), 1994.

1149 Meskhidze, N., Chameides, W. L., and Nenes, A.: Dust and pollution: A recipe for enhanced ocean fertilization?,
1150 *Journal of Geophysical Research: Atmospheres*, 110, 10.1029/2004JD005082, 2005.

1151 Moore, C. M., Mills, M. M., Arrigo, K. R., Berman-Frank, I., Bopp, L., Boyd, P. W., Galbraith, E. D., Geider, R.
1152 J., Guieu, C., Jaccard, S. L., Jickells, T. D., La Roche, J., Lenton, T. M., Mahowald, N. M., Maranon, E.,
1153 Marinov, I., Moore, J. K., Nakatsuka, T., Oschlies, A., Saito, M. A., Thingstad, T. F., Tsuda, A., and Ulloa, O.:

1154 Processes and patterns of oceanic nutrient limitation, *Nature Geoscience*, 6, 701-710, 10.1038/ngeo1765, 2013.

1155 Moreno, N., Querol, X., Andrés, J. M., Stanton, K., Towler, M., Nugteren, H., Janssen-Jurkovicová, M., and Jones,

1156 R.: Physico-chemical characteristics of European pulverized coal combustion fly ashes, *Fuel*, 84, 1351-1363,

1157 2005.

1158 Myriokefalitakis, S., Ito, A., Kanakidou, M., Nenes, A., Krol, M. C., Mahowald, N. M., Scanza, R. A., Hamilton,

1159 D. S., Johnson, M. S., Meskhidze, N., Kok, J. F., Guieu, C., Baker, A. R., Jickells, T. D., Sarin, M. M., Bikkina,

1160 S., Shelley, R., Bowie, A., Perron, M. M. G., and Duce, R. A.: Reviews and syntheses: the GESAMP

1161 atmospheric iron deposition model intercomparison study, *Biogeosciences*, 15, 6659-6684, 2018.

1162 Nishioka, J. and Obata, H.: Dissolved iron distribution in the western and central subarctic Pacific: HNLC water

1163 formation and biogeochemical processes, *Limnology and Oceanography*, 62, 2004-2022,

1164 <https://doi.org/10.1002/lno.10548>, 2017.

1165 Oakes, M., Ingall, E. D., Lai, B., Shafer, M. M., Hays, M. D., Liu, Z. G., Russell, A. G., and Weber, R. J.: Iron

1166 Solubility Related to Particle Sulfur Content in Source Emission and Ambient Fine Particles, *Environmental*

1167 *Science & Technology*, 46, 6637-6644, 2012.

1168 Oliveira, C. M., Machado, C. M., Duarte, G. W., and Peterson, M.: Beneficiation of pyrite from coal mining,

1169 *Journal of Cleaner Production*, 139, 821-827, <https://doi.org/10.1016/j.jclepro.2016.08.124>, 2016.

1170 Ooki, A., Nishioka, J., Ono, T., and Noriki, S.: Size dependence of iron solubility of Asian mineral dust particles,

1171 *Journal of Geophysical Research: Atmospheres*, 114, 10.1029/2008JD010804, 2009.

1172 Panda, P. P., Aswini, M. A., Bhatt, P., Srimuruganandam, B., Peketi, A., and Kumar, A.: Bioactive Trace Elements'

1173 Composition and Their Fractional Solubility in Aerosols from the Arabian Sea during the Southwest Monsoon,

1174 *ACS Earth Space Chem.*, 6, 1969-1981, 10.1021/acsearthspacechem.2c00067, 2022.

1175 Patil, R. S., Kumar, R., Menon, R., Shah, M. K., and Sethi, V.: Development of particulate matter speciation

1176 profiles for major sources in six cities in India, *Atmospheric Research*, 132-133, 1-11,

1177 <https://doi.org/10.1016/j.atmosres.2013.04.012>, 2013.

1178 Perron, M. M. G., Fietz, S., Hamilton, D. S., Ito, A., Shelley, R. U., and Tang, M.: Preface to the inter-journal

1179 special issue "RUSTED: Reducing Uncertainty in Soluble aerosol Trace Element Deposition", *Atmospheric*

1180 *Measurement Techniques*, 17, 165-166, 10.5194/amt-17-165-2024, 2024.

1181 Perron, M. M. G., Meyerink, S., Corkill, M., Strzelec, M., Proemse, B. C., Gault-Ringold, M., Sanz Rodriguez,

1182 E., Chase, Z., and Bowie, A. R.: Trace elements and nutrients in wildfire plumes to the southeast of Australia,

1183 *Atmospheric Research*, 270, 106084, <https://doi.org/10.1016/j.atmosres.2022.106084>, 2022.

1184 Ram, L. C., Tripathi, P. S. M., and Mishra, S. P.: Mössbauer spectroscopic studies on the transformations of iron-

1185 bearing minerals during combustion of coals: Correlation with fouling and slagging, *Fuel Processing*

1186 *Technology*, 42, 47-60, [https://doi.org/10.1016/0378-3820\(94\)00111-6](https://doi.org/10.1016/0378-3820(94)00111-6), 1995.

1187 Rathod, S. D., Hamilton, D. S., Mahowald, N. M., Klimont, Z., Corbett, J. J., and Bond, T. C.: A Mineralogy-

1188 Based Anthropogenic Combustion-Iron Emission Inventory, *Journal of Geophysical Research: Atmospheres*,

1189 125, e2019JD032114, <https://doi.org/10.1029/2019JD032114>, 2020.

1190 Rathod, S. D., Hamilton, D. S., Nino, L., Kreidenweis, S. M., Bian, Q., Mahowald, N. M., Alastuey, A., Querol,

1191 X., Paytan, A., Artaxo, P., Herut, B., Gaston, C., Prospero, J., Chellam, S., Hueglin, C., Varrica, D., Dongarra,

1192 G., Cohen, D. D., Smichowski, P., Gomez, D., Lambert, F., Barraza, F., Bergametti, G., Rodríguez, S.,

1193 Gonzalez-Ramos, Y., Hand, J., Kyllönen, K., Hakola, H., Chuang, P., Hopke, P. K., Harrison, R. M., Martin,

1194 R. V., Walsh, B., Weagle, C., Maenhaut, W., Morera-Gómez, Y., Chen, Y.-C., Pierce, J. R., and Bond, T. C.:

1195 Constraining Present-Day Anthropogenic Total Iron Emissions Using Model and Observations, *Journal of*

1196 *Geophysical Research: Atmospheres*, 129, e2023JD040332, <https://doi.org/10.1029/2023JD040332>, 2024.

1197 Riahi, K., van Vuuren, D. P., Kriegler, E., Edmonds, J., O'Neill, B. C., Fujimori, S., Bauer, N., Calvin, K., Dellink,

1198 R., Fricko, O., Lutz, W., Popp, A., Cuaresma, J. C., Kc, S., Leimbach, M., Jiang, L., Kram, T., Rao, S.,
1199 Emmerling, J., Ebi, K., Hasegawa, T., Havlik, P., Humpenöder, F., Da Silva, L. A., Smith, S., Stehfest, E.,
1200 Bosetti, V., Eom, J., Gernaat, D., Masui, T., Rogelj, J., Strefler, J., Drouet, L., Krey, V., Luderer, G., Harmsen,
1201 M., Takahashi, K., Baumstark, L., Doelman, J. C., Kainuma, M., Klimont, Z., Marangoni, G., Lotze-Campen,
1202 H., Obersteiner, M., Tabeau, A., and Tavoni, M.: The Shared Socioeconomic Pathways and their energy, land
1203 use, and greenhouse gas emissions implications: An overview, *Global Environmental Change*, 42, 153-168,
1204 <https://doi.org/10.1016/j.gloenvcha.2016.05.009>, 2017.

1205 Ridley, D. A., Heald, C. L., Kok, J. F., and Zhao, C.: An observationally constrained estimate of global dust aerosol
1206 optical depth, *Atmos. Chem. Phys.*, 16, 15097-15117, 10.5194/acp-16-15097-2016, 2016.

1207 Rodríguez, S., Prospero, J. M., López-Darias, J., García-Alvarez, M.-I., Zuidema, P., Nava, S., Lucarelli, F.,
1208 Gaston, C. J., Galindo, L., and Sosa, E.: Tracking the changes of iron solubility and air pollutants traces as
1209 African dust transits the Atlantic in the Saharan dust outbreaks, *Atmospheric Environment*, 246, 118092,
1210 <https://doi.org/10.1016/j.atmosenv.2020.118092>, 2021.

1211 Sakata, K., Kurisu, M., Takeichi, Y., Sakaguchi, A., Tanimoto, H., Tamenori, Y., Matsuki, A., and Takahashi, Y.:
1212 Iron (Fe) speciation in size-fractionated aerosol particles in the Pacific Ocean: The role of organic
1213 complexation of Fe with humic-like substances in controlling Fe solubility, *Atmos. Chem. Phys.*, 22, 9461-
1214 9482, 10.5194/acp-22-9461-2022, 2022.

1215 Scanza, R. A., Hamilton, D. S., Perez Garcia-Pando, C., Buck, C., Baker, A., and Mahowald, N. M.: Atmospheric
1216 processing of iron in mineral and combustion aerosols: development of an intermediate-complexity
1217 mechanism suitable for Earth system models, *Atmospheric Chemistry and Physics*, 18, 14175-14196,
1218 10.5194/acp-18-14175-2018, 2018.

1219 Schmidl, C., Marr, I. L., Caseiro, A., Kotianová, P., Berner, A., Bauer, H., Kasper-Giebl, A., and Puxbaum, H.:
1220 Chemical characterisation of fine particle emissions from wood stove combustion of common woods growing
1221 in mid-European Alpine regions, *Atmospheric Environment*, 42, 126-141,
1222 <https://doi.org/10.1016/j.atmosenv.2007.09.028>, 2008.

1223 Schroth, A. W., Crusius, J., Sholkovitz, E. R., and Bostick, B. C.: Iron solubility driven by speciation in dust
1224 sources to the ocean, *Nature Geoscience*, 2, 337-340, 10.1038/ngeo501, 2009.

1225 Seo, H. and Kim, G.: Anthropogenic Iron Invasion into the Ocean: Results from the East Sea (Japan Sea),
1226 *Environmental Science & Technology*, 57, 10745-10753, 10.1021/acs.est.3c01084, 2023.

1227 Shi, Z. B., Woodhouse, M. T., Carslaw, K. S., Krom, M. D., Mann, G. W., Baker, A. R., Savov, I., Fones, G. R.,
1228 Brooks, B., Drake, N., Jickells, T. D., and Benning, L. G.: Minor effect of physical size sorting on iron
1229 solubility of transported mineral dust, *Atmospheric Chemistry and Physics*, 11, 8459-8469, 10.5194/acp-11-
1230 8459-2011, 2011.

1231 Silva, V. S., Silva, J. S., Costa, B. d. S., Labes, C., and Oliveira, R. M. P. B.: Preparation of glaze using electric-
1232 arc furnace dust as raw material, *Journal of Materials Research and Technology*, 8, 5504-5514,
1233 <https://doi.org/10.1016/j.jmrt.2019.09.018>, 2019.

1234 Souza, C. A. C. D., Machado, A. T., Lima, L. R. P. d. A., and Cardoso, R. J. C.: Stabilization of electric-arc furnace
1235 dust in concrete, *Materials Research*, 13, 513-519, 2010.

1236 Srinivas, B., Sarin, M. M., and Kumar, A.: Impact of anthropogenic sources on aerosol iron solubility over the
1237 Bay of Bengal and the Arabian Sea, *Biogeochemistry*, 110, p.257-268, 2012.

1238 Stathopoulos, V. N., Papandreou, A., Kanellopoulou, D., and Stournaras, C. J.: Structural ceramics containing
1239 electric arc furnace dust, *Journal of hazardous materials*, 262, 91-99,
1240 <https://doi.org/10.1016/j.jhazmat.2013.08.028>, 2013.

1241 Stoner, O., Lewis, J., Martínez, I. L., Gumy, S., Economou, T., and Adair-Rohani, H.: Household cooking fuel

1242 estimates at global and country level for 1990 to 2030, *Nature Communications*, 12, 5793, 10.1038/s41467-
1243 021-26036-x, 2021.

1244 Tagliabue, A., Aumont, O., and Bopp, L.: The impact of different external sources of iron on the global carbon
1245 cycle, *Geophys. Res. Lett.*, 41, 920-926, <https://doi.org/10.1002/2013GL059059>, 2014.

1246 Tagliabue, A., Bowie, A. R., Boyd, P. W., Buck, K. N., Johnson, K. S., and Saito, M. A.: The integral role of iron
1247 in ocean biogeochemistry, *Nature*, 543, 51-59, 10.1038/nature21058, 2017.

1248 Tang, M., Perron, M. M. G., Baker, A. R., Li, R., Bowie, A. R., Buck, C. S., Kumar, A., Shelley, R., Ussher, S. J.,
1249 Clough, R., Meyerink, S., Panda, P. P., Townsend, A. T., and Wyatt, N.: Measurement of soluble aerosol trace
1250 elements: inter-laboratory comparison of eight leaching protocols, *Atmos. Meas. Tech.*, 18, 6125-6141,
1251 10.5194/amt-18-6125-2025, 2025.

1252 Taylor, S. R. and McLennan, S. M.: The geochemical evolution of the continental crust, *Reviews of Geophysics*,
1253 33, 241-265, 1995.

1254 Tegler, L. A., Sherry, A. M., Herckes, P., Romaniello, S. J., and Anbar, A. D.: Up in Smoke: Most Aerosolized Fe
1255 From Biomass Burning Does Not Derive From Foliage, *Global Biogeochemical Cycles*, 37, e2023GB007796,
1256 <https://doi.org/10.1029/2023GB007796>, 2023.

1257 Turnock, S. T., Allen, R. J., Andrews, M., Bauer, S. E., Deushi, M., Emmons, L., Good, P., Horowitz, L., John, J.
1258 G., Michou, M., Nabat, P., Naik, V., Neubauer, D., O'Connor, F. M., Oliv  , D., Oshima, N., Schulz, M., Sellar,
1259 A., Shim, S., Takemura, T., Tilmes, S., Tsigaridis, K., Wu, T., and Zhang, J.: Historical and future changes in
1260 air pollutants from CMIP6 models, *Atmospheric Chemistry and Physics*, 20, 14547-14579, 10.5194/acp-20-
1261 14547-2020, 2020.

1262 van Marle, M. J. E., Kloster, S., Magi, B. I., Marlon, J. R., Daniau, A. L., Field, R. D., Arneth, A., Forrest, M.,
1263 Hantson, S., Kehrwald, N. M., Knorr, W., Lasslop, G., Li, F., Mangeon, S., Yue, C., Kaiser, J. W., and van der
1264 Werf, G. R.: Historic global biomass burning emissions for CMIP6 (BB4CMIP) based on merging satellite
1265 observations with proxies and fire models (1750–2015), *Geoscientific Model Development*, 10, 3329-3357,
1266 10.5194/gmd-10-3329-2017, 2017.

1267 Vieira, C. M. F., Sanchez, R., Monteiro, S. N., Lalla, N., and Quaranta, N.: Recycling of electric arc furnace dust
1268 into red ceramic, *Journal of Materials Research and Technology*, 2, 88-92,
1269 <https://doi.org/10.1016/j.jmrt.2012.09.001>, 2013.

1270 Wang, R., Balkanski, Y., Boucher, O., Bopp, L., Chappell, A., Ciais, P., Hauglustaine, D., Pe  uelas, J., and Tao,
1271 S.: Sources, transport and deposition of iron in the global atmosphere, *Atmospheric Chemistry and Physics*,
1272 15, 6247-6270, 10.5194/acp-15-6247-2015, 2015.

1273 Ward, C. R.: Analysis, origin and significance of mineral matter in coal: An updated review, *International Journal*
1274 *of Coal Geology*, 165, 1-27, <https://doi.org/10.1016/j.coal.2016.07.014>, 2016.

1275 Watson, J. G., Chow, J. C., and Houck, J. E.: PM2.5 chemical source profiles for vehicle exhaust, vegetative
1276 burning, geological material, and coal burning in Northwestern Colorado during 1995, *Chemosphere*, 43,
1277 1141-1151, [https://doi.org/10.1016/S0045-6535\(00\)00171-5](https://doi.org/10.1016/S0045-6535(00)00171-5), 2001.

1278 Winton, V. H. L., Bowie, A. R., Curran, M. A., and Moy, A. D.: Enhanced Deposition of Atmospheric Soluble
1279 Iron by Intrusions of Marine Air Masses to East Antarctica, *Journal of Geophysical Research: Atmospheres*,
1280 127, e2022JD036586, <https://doi.org/10.1029/2022JD036586>, 2022.

1281 Wu, C., Lin, Z., and Liu, X.: The global dust cycle and uncertainty in CMIP5 (Coupled Model Intercomparison
1282 Project phase 5) models, *Atmospheric Chemistry and Physics*, 20, 10401-10425, 10.5194/acp-20-10401-2020,
1283 2020.

1284 Wu, D., Li, Q., Ding, X., Sun, J., Li, D., Fu, H., Teich, M., Ye, X., and Chen, J.: Primary Particulate Matter Emitted
1285 from Heavy Fuel and Diesel Oil Combustion in a Typical Container Ship: Characteristics and Toxicity,

1286 Environmental Science & Technology, 52, 12943-12951, 10.1021/acs.est.8b04471, 2018.

1287 Wu, H.-Y., Hsieh, C.-C., and Ho, T.-Y.: Trace metal dissolution kinetics of East Asian size-fractionated aerosols
1288 in seawater: The effect of a model siderophore, Marine Chemistry, 254, 104277,
1289 <https://doi.org/10.1016/j.marchem.2023.104277>, 2023.

1290 Xia, D. K. and Picklesi, C. A.: Microwave caustic leaching of electric arc furnace dust, Minerals Engineering, 13,
1291 79-94, [https://doi.org/10.1016/S0892-6875\(99\)00151-X](https://doi.org/10.1016/S0892-6875(99)00151-X), 2000.

1292 Ye, L., Peng, Z., Ye, Q., Wang, L., Augustine, R., Perez, M., Liu, Y., Liu, M., Tang, H., Rao, M., Li, G., and Jiang,
1293 T.: Toward environmentally friendly direct reduced iron production: A novel route of comprehensive
1294 utilization of blast furnace dust and electric arc furnace dust, Waste Management, 135, 389-396,
1295 <https://doi.org/10.1016/j.wasman.2021.08.045>, 2021.

1296 Zhang, H., Wang, S., Hao, J., Wan, L., Jiang, J., Zhang, M., Mestl, H. E. S., Alnes, L. W. H., Aunan, K., and
1297 Mellouki, A. W.: Chemical and size characterization of particles emitted from the burning of coal and wood
1298 in rural households in Guizhou, China, Atmospheric Environment, 51, 94-99,
1299 <https://doi.org/10.1016/j.atmosenv.2012.01.042>, 2012.

1300 Zhang, H., Li, R., Dong, S., Wang, F., Zhu, Y., Meng, H., Huang, C., Ren, Y., Wang, X., Hu, X., Li, T., Peng, C.,
1301 Zhang, G., Xue, L., Wang, X., and Tang, M.: Abundance and Fractional Solubility of Aerosol Iron During
1302 Winter at a Coastal City in Northern China: Similarities and Contrasts Between Fine and Coarse Particles,
1303 Journal of Geophysical Research: Atmospheres, 127, e2021JD036070,
1304 <https://doi.org/10.1029/2021JD036070>, 2022.

1305 Zhang, T., Liu, J., Xiang, Y., Liu, X., Zhang, J., Zhang, L., Ying, Q., Wang, Y., Wang, Y., Chen, S., Chai, F., and
1306 Zheng, M.: Quantifying anthropogenic emission of iron in marine aerosol in the Northwest Pacific with
1307 shipborne online measurements, Science of The Total Environment, 912, 169158,
1308 <https://doi.org/10.1016/j.scitotenv.2023.169158>, 2024.

1309